Automatica 159 (2024) 109922

Contents lists available at ScienceDirect

Automatica

journal homepage: www.elsevier.com/locate/automatica

Adaptive control of a VTOL uncrewed aerial vehicle for high-performance aerobatic flight☆

Ying Chen [a,*], Néstor O. Pérez-Arancibia [a,b,*]

[a] Department of Aerospace and Mechanical Engineering, University of Southern California (USC), Los Angeles, CA 90089-1453, USA
[b] School of Mechanical and Materials Engineering, Washington State University (WSU), Pullman, WA 99164-2920, USA

ARTICLE INFO

Article history:
Received 18 September 2019
Received in revised form 11 March 2021
Accepted 22 August 2021
Available online 10 November 2023

Keywords:
Aerial robotics
Adaptive control
VTOL UAV
Aerobatic maneuvers
Time-varying actuator dynamics

ABSTRACT

We present two adaptive control methods conceived to enable a *vertical take-off and landing* (VTOL) *uncrewed aerial vehicle* (UAV) to perform a class of aerobatic maneuvers in the presence of aerodynamic-coefficient and torque-latency variations induced by changes of the local flow fields during high-speed aerobatic flight. First, we introduce a *linear time-varying* (LTV) dynamical model, which is assumed to have unknown time-dependent parameters, to describe the aerodynamic effects acting on the actuation dynamics of the system. Then, we present the design of a Lyapunov-based adaptive control scheme aimed to compensate for undesired behavior of the LTV actuator dynamics, according to which we derive the control and adaptation laws from a single Lyapunov candidate function. Next, we propose a modular adaptive control scheme to address the same problem, but in which the adaptation law is specified separately from that of the controller. We use modern nonlinear theory to deduce and analyze the conditions that guarantee the global asymptotic stability of both adaptive control strategies. In order to exemplify the controller synthesis procedures, we implemented both adaptive control methods on a quadrotor UAV to perform three different types of aerobatic-flight maneuvers—namely, triple flips, Pugachev's *cobras*, and mixed flips. The obtained experimental results provide compelling evidence of the effectiveness of the two proposed methods to compensate for the undesired effects induced by aerodynamic-coefficient and torque-latency variations. Furthermore, the experimental data demonstrate that both adaptive schemes significantly improve the flight performance of the quadrotor UAV during the execution of aerobatic maneuvers, compared to those achieved with a controller that disregards the LTV actuator dynamics induced by high-speed aerodynamic effects. The suitability of the time-varying approach used to model the influence of high-speed local flow fields on the dynamics of the controlled UAV was indirectly validated through data obtained during the aerobatic-flight experiments presented here.

1. Introduction

In recent years, *vertical take-off and landing* (VTOL) *uncrewed aerial vehicles* (UAVs) have attracted significant research attention and been used in a wide range of applications, including field surveillance, search and rescue, aerial filming, and agriculture spraying. The most salient characteristic of VTOL UAVs is that they are, typically, fully actuated in attitude motion and under-actuated in translational motion (Hua, Hamel, Morin, & Samson, 2009; Lee, 2012); examples of this type of system are uncrewed versions of the helicopter, the quadrotor, and the ducted-fan aircraft. However, despite their increasing popularity, artificial aerial vehicles are still outmatched by aerial animals regarding autonomy and flight capabilities. Specifically, VTOL UAVs do not exhibit maneuver abilities comparable to those of natural flyers, which can capture prey in flight, escape predators, and avoid obstacles at extremely high velocities (Dudley, 2002). We believe that for VTOL UAVs to achieve full autonomy, similar extreme flight capabilities must be developed because these are required to accomplish missions and survive in real-life unstructured environments full of unexpected challenges.

From a primarily theoretical perspective, a significant amount of research on attitude and position control of VTOL UAVs, under several different flight conditions, has been published. For example, studies on position tracking control of VTOL flyers in the presence of aerodynamic disturbances are presented in Cabecinhas, Cunha, and Silvestre (2015), Hua et al. (2009), and Roberts and Tayebi (2011); a global trajectory-tracking controller for

☆ This research was partially supported by the *National Science Foundation* (NSF) of the USA through NRI Award 1528110, and the USC Viterbi School of Engineering through a graduate fellowship to Y. Chen and a start-up fund to N. O. Pérez-Arancibia. The material in this paper was not presented at any conference. This paper was recommended for publication in revised form by Associate Editor Abdelhamid Tayebi under the direction of Editor Thomas Parisini.

* Corresponding author.
E-mail addresses: chen061@usc.edu (Y. Chen), n.perezarancibia@wsu.edu (N.O. Pérez-Arancibia).

https://doi.org/10.1016/j.automatica.2021.109922
0005-1098/

UAVs without translational velocity measurements is introduced in Abdessameud and Tayebi (2010); a geometric method devised to achieve *quasi* global position-tracking control of a quadrotor UAV is presented and discussed in Lee, Leok, and McClamroch (2010); and, an adaptive position controller designed to deal with the loss-of-thrust situation caused by component failure is presented in Dydek, Annaswamy, and Lavretsky (2013). However, none of those research efforts considered the problem of controller synthesis for high-speed aerobatic flight; furthermore, the only verifications of those control methods were obtained through either simulations or simple experiments in which the tested UAVs remained in a near-hovering state characterized by small attitude-angle variations and slow angular velocities.[1]

On the other hand, many publications, which do not address the theoretical complexities associated with high-speed aerodynamic phenomena, have presented experimentally-driven research aimed at enlarging the flight envelope of VTOL UAVs from steady hovering to aerobatic flight characterized by large attitude-angle variations and high angular velocities.[2] For instance, in the experiments presented in Lupashin and D'Andrea (2012) and Mellinger, Michael, and Kumar (2012), quadrotor UAVs were demonstrated to perform aerobatic maneuvers, such as multi-flips and fast flights through tilted windows, employing an *iterative learning control* (ILC) strategy. However, stability analyses of the closed-loop systems and proofs of convergence of the learning parameters are not provided; therefore, it is not entirely clear what conditions are required for those flight controllers to function adequately. Additionally, ILC-based methods are not suitable to most real-life unpredictable scenarios in which a controlled UAV does not have a second opportunity to execute an aerobatic maneuver after a first attempt. In Chen and Pérez-Arancibia (2016, 2017, 2020), we presented methods for synthesizing controllers that enable high-speed aerobatic quadrotor flight (multi-flips in specific) and optimize the corresponding tracking performance; the resulting controllers were validated through both rigorous stability analyses and compelling experimental results. However, in the research presented in those articles, we did not consider the aerodynamic effects affecting the system, which are magnified during extreme flight conditions, as we assumed that the near-hovering flight assumption was entirely valid.

The rapid translational and rotational motions required by a controlled UAV to perform aerobatic flight drastically increase the relative velocities, with respect to those experienced during normal hovering flight, of the local incoming flows faced by the propellers of the flyer.[3] This phenomenon inevitably affects the actuation dynamics of the system because the aerodynamic coefficients of the propellers and the latency of the control torque become time-varying, as discussed in Chen and Pérez-Arancibia (2018, 2019). In relation to this observation, it is important to note that aerial animals exhibit remarkable flight abilities while performing maneuvers in the presence of complex surrounding flow fields. For example, the fruit fly (*Drosophila melanogaster*) is able to perform a 90° banked turn in about 50 ms with a yaw acceleration of as high as $10^5\,^\circ\cdot\,\mathrm{s}^{-2}$ (Fry, Sayaman, & Dickinson, 2003); the barn swallow (*Hirundo rustica*) has been recorded executing roll turns at rates of as high as $5\times10^3\,^\circ\cdot\,\mathrm{s}^{-1}$ (Shyy, Lian, Tang, Viieru, & Liu, 2007); and, the magnificent hummingbird (*Eugenes fulgens*) has been recorded performing escape maneuvers with a maximum roll rate of more than $4\times10^3\,^\circ\cdot\,\mathrm{s}^{-1}$ in about 0.25 s (Cheng, et al., 2016). In fact, most aerial animals are able to execute complex high-speed controlled aerobatic flights without stalling in the air or crashing to the ground, which clearly indicates that there still exists a performance gap between artificial and natural flyers.

Consistent with biological observations, we believe that for VTOL UAVs to acquire maneuver abilities comparable to those exhibited by natural flyers, it is essential to develop methods for synthesizing flight controllers that explicitly consider the aerodynamic effects generated by high-speed time-varying surrounding flow fields. Unfortunately, to date, most research on dynamic modeling and control of VTOL UAVs has overly simplified or neglected the aerodynamic effects affecting the controlled systems by assuming time-invariant flow fields, typically described using constant aerodynamic coefficients (Bangura & Mahony, 2012; Bristeau, Martin, Salaün, & Petit, 2009; Mahony, Kumar, & Corke, 2012). This approach is reasonable and sufficiently accurate in the near-hovering flight case, characterized by slow translational and rotational velocities with small attitude-angle variations. However, the assumption that the aerodynamic coefficients of the propellers are constant becomes highly improbable in the aerobatic flight case. Furthermore, fluctuations of the loading moments acting on the propellers, caused by high-speed variations of the surrounding local flow fields and associated aerodynamic parameters, can rapidly change the torque latency and introduce another time-varying term into the actuator dynamics. To address these issues, in Chen and Pérez-Arancibia (2018, 2019), we proposed a *linear time-varying* (LTV) actuator model that explicitly accounts for the effects of complex flow-field variations. Based on that model, we developed an adaptive control solution capable of compensating for undesirable behavior produced by the time-varying dynamics of the modeled actuators, thus significantly improving the empirical flight performance of the controlled VTOL UAV compared to those obtained with prior *linear time-invariant* (LTI) solutions. However, we did not provide a rigorous stability analysis of the closed-loop system. Similarly, in the research presented in Bisheban and Lee (2021), a neural-network-based model was applied to describe the external wind disturbances affecting a UAV during flight; the corresponding experimental control results, nonetheless, do not exhibit aerobatic flight performances comparable to those reported in previous experimental papers (Lupashin & D'Andrea, 2012; Mellinger et al., 2012).

The main contribution of this article is the introduction of two different adaptive control schemes developed to compensate for the LTV actuator dynamics with unknown parameters that we use to describe the time-varying aerodynamic effects affecting a VTOL UAV during extreme aerobatic flight. Also, we provide and discuss a mathematically-rigorous stability analysis of the closed-loop adaptive systems. To begin, we introduce an LTV model of torque to account for the aerodynamic variations affecting the actuator dynamics of the controlled VTOL UAV. Then, we present and discuss the processes of synthesis and analysis of the two proposed adaptive control methods. We derived the first method using Lyapunov's nonlinear techniques, according to which the synthesized control and adaptation laws are generated from a single *proto*-Lyapunov function to guarantee the asymptotic stability of the closed-loop system. The second method, inspired by ideas in Krstić, Kanellakopoulos, and Kokotović (1995), is based on a modular adaptive control scheme, according to which the controller and adaptation laws are designed separately. We conceived the two proposed adaptive schemes with the main control objective of ensuring closed-loop stability while achieving high flight performance.

[1] The term *small attitude angle* indicates that the angle between the vertical upward direction and the direction of the thrust force generated by the controlled VTOL UAV is less than 90°; the term *slow angular velocity* indicates that the magnitude of the controlled UAV's velocity is less than $500^\circ\cdot\,\mathrm{s}^{-1}$.

[2] The term *large attitude angle* refers to an angle between the vertical upward direction and the direction of the thrust force generated by the controlled VTOL UAV that is larger than 90°; the term *high angular velocity* refers to a velocity magnitude that is larger than $500^\circ\cdot\,\mathrm{s}^{-1}$.

[3] In this paper, we assume that the thrust force acting on the controlled VTOL UAV is entirely generated by its rotating propellers.

Because we expect the proposed controllers to drive VTOL UAVs while executing aggressive aerobatic maneuvers in fractions of a second, it is crucial to counteract the adverse effects affecting the transient performance of the system even before the adaptive parameters have converged. To test this capability, we experimentally implemented both adaptive control schemes on a quadrotor UAV to perform three different types of representative maneuvers: triple-flips, Pugachev's cobras, and mixed flips. The empirical data univocally indicate a significant improvement in flight-control performance in all the experimental cases, compared to the results obtained with a high-performance LTI controller that disregards the time-varying characteristic of the actuator dynamics. Specifically, both adaptive control methods drastically reduced undesired angular-velocity oscillations and overshoots. Last, we compare the experimental control errors obtained with the two proposed controllers, which achieve similar performance values.

For clarity and completeness, we briefly state the research contributions presented in this article relative to our prior publications. In the research presented in Chen and Pérez-Arancibia (2016, 2017, 2020), we did not consider the aerodynamic effects acting on the actuator dynamics of the controlled VTOL UAVs during aerobatic flight and only used the nominal open-loop dynamics for controller synthesis. Moreover, in the research presented in Chen and Pérez-Arancibia (2018, 2019), we did not provide rigorous stability analyses of the resulting closed-loop systems. In clear contrast with our previous work, the approach introduced in this article explicitly consideres the high-speed time-varying aerodynamic effects affecting the actuation of the controlled VTOL UAVs when developing the two proposed methods for synthesizing adaptive controllers. Furthermore, here, we present rigorous stability analyses and provide the conditions that guarantee the global asymptotic stability of the closed-loop systems.

2. Preliminaries

2.1. Notation

We denote scalars using regular lowercase or uppercase symbols, e.g., a or Φ; we denote vectors using bold lowercase symbols, e.g., $\boldsymbol{a}$; we denote matrices using bold uppercase symbols, e.g., $\boldsymbol{A}$; and, we denote quaternions using bar-crossed bold lowercase symbols, e.g., $\bar{\boldsymbol{q}}$. The symbol $*$ denotes the quaternion product, e.g., $\bar{\boldsymbol{q}} * \bar{\boldsymbol{p}}$. The symbol $\succ$ (or the nonstrict form $\succeq$) denotes a component-wise inequality between vectors and a matrix inequality between Hermitian definite matrices. For a set $\mathcal{S}$, the interior of $\mathcal{S}$ is denoted by $\mathring{\mathcal{S}}$, and the boundary of $\mathcal{S}$ is denoted by $\partial\mathcal{S}$. We write the difference between two sets as $\mathcal{A} \setminus \mathcal{B} = \{\boldsymbol{x} : \boldsymbol{x} \in \mathcal{A} \text{ and } \boldsymbol{x} \notin \mathcal{B}\}$. The operator $\lambda_{\min}\{\cdot\}$ extracts the minimum eigenvalue of a symmetric matrix; the operator $|\cdot|$ computes the absolute value of a scalar; the operator $|\cdot|_2$ computes the Euclidean norm of a vector; the operator $\|\cdot\|_{\mathrm{F}}$ computes the Frobenius norm of a matrix; the operator $\mathrm{tr}\{\cdot\}$ computes the trace of a square matrix; the operator $\mathrm{sgn}\{\cdot\}$ extracts the sign of a real number; and, the symbol ∇ denotes the *del* operator. Last, we denote the set of real numbers using the symbol $\mathbb{R}$, any generic identity matrix with $\boldsymbol{I}$, and time with t. In particular, $t = t_0$ indicates the time at which a given aerobatic maneuver starts.

2.2. A class of aerobatic maneuvers

The aerobatic maneuvers of the class considered in this paper are defined by fast sequential rotations about a single axis or multiple axes, during which the translational motion of the controlled VTOL UAV remains in free fall and open loop. The rotation axes of the sequential subrotations used in an aerobatic maneuver are defined by a sequence of k body-fixed unit vectors sorted in the order of occurrence as $\{\boldsymbol{a}_1, \boldsymbol{a}_2, \ldots, \boldsymbol{a}_k\}$, and the sequence of rotation angles for the corresponding subrotations is denoted by $\{\Phi_1, \Phi_2, \ldots, \Phi_k\}$. Furthermore, the sequence of maximum angular speeds of the corresponding subrotations is denoted by $\{\dot{\Phi}_{\max,1}, \dot{\Phi}_{\max,2}, \ldots, \dot{\Phi}_{\max,k}\}$. Accordingly, the angular-velocity reference $\boldsymbol{\omega}_{\mathrm{d}}$ is composed of a sequence of k signals $\{\boldsymbol{\omega}_{\mathrm{d},1}, \boldsymbol{\omega}_{\mathrm{d},2}, \ldots, \boldsymbol{\omega}_{\mathrm{d},k}\}$, sorted in order of occurrence. We formalize these ideas through a definition.

Definition 1. The aerobatic maneuvers for VTOL UAVs of the generic class considered in this paper start from an initial attitude corresponding to a thrust force with a direction that points vertically upward and end at a final state with exactly the same attitude as that of the initial state. In the most generic case, a maneuver is composed of a sequence of subrotations. During each subrotation, the vehicle rotates about the corresponding body-fixed axis $\boldsymbol{a}_i$, thus accumulating an additional rotation angle Φ_i, without surpassing the maximum rotation speed $\dot{\Phi}_{\max,i}$, for $i \in \{1, 2, \ldots, k\}$. The reference signal for each subrotation, $\boldsymbol{\omega}_{\mathrm{d},i}(t)$, for $i \in \{1, 2, \ldots, k\}$, starts and ends at zero. The complete angular-velocity reference expressed in the body-fixed frame defined in Section 3, $\boldsymbol{\omega}_{\mathrm{d}}(t)$, is chosen to be continuously differentiable.

From Definition 1, it follows that $\int_{t_{\mathrm{i},i}}^{t_{\mathrm{f},i}} \left|\boldsymbol{\omega}_{\mathrm{d},i}(t)\right|_2 dt = \Phi_i$, where $t_{\mathrm{i},i}$ and $t_{\mathrm{f},i}$ are the initial and final times of the subrotation i, and $\max_{t\in[t_{\mathrm{i},i}:t_{\mathrm{f},i}]} \left\{\left|\boldsymbol{\omega}_{\mathrm{d},i}(t)\right|_2\right\} = \dot{\Phi}_{\max,i}$. The translational motion is assumed to be the free-fall state because the direction of the thrust force changes extremely fast[4] between the upward and downward orientations, and gravity is assumed to be the only external force acting on the UAV. Translational drift on the horizontal plane may exist but remains bounded due to the extremely short duration of the maneuver.

2.3. The aerobatic-maneuver process

The entire process of an aerobatic maneuver can be divided into three phases: *climb*, *maneuver execution* (ME); and *descent* and *restabilization* (DR). At the start, the controlled UAV hovers at a preset position. After receiving the command to perform the maneuver, the UAV starts climbing a preset distance to reach an initial upward speed, which helps to reduce the descending speed at the end of the maneuver. Subsequently, the vehicle enters the ME phase and executes the maneuver while its translational motion stays in the pure free-fall state. After the maneuver is completed, the direction of the thrust force generated by the propellers returns to the upward orientation, and the vehicle restabilizes its attitude to hover and stop descending. More details regarding this process can be found in Chen and Pérez-Arancibia (2020). During the climb and DR phases, the VTOL UAV stays at a near-hovering attitude state, which can be regulated using simple control laws. Consistently, here, we focus on the synthesis of controllers for the ME phase. The stability and performance analyses of the controller while switching between phases can be found in Chen and Pérez-Arancibia (2020).

3. Problem statement

3.1. Dynamics of a VTOL UAV with LTV actuation

An example of a VTOL UAV, a 28-g quadrotor aircraft, is shown in Fig. 1. In this case, the arbitrarily-chosen inertial frame of

[4] During a maneuver, which is completed in less than 1 s, a controlled UAV produces angular speeds with values greater than $1000^\circ \cdot \mathrm{s}^{-1}$.

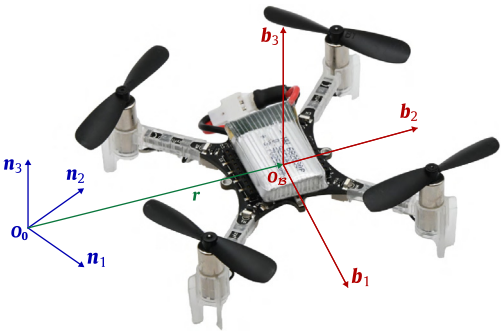

Fig. 1. A quadrotor UAV and frames of reference. Here, $\mathcal{N} = \{\boldsymbol{O_0}, \boldsymbol{n}_1, \boldsymbol{n}_2, \boldsymbol{n}_3\}$ denotes the inertial frame, $\mathcal{B} = \{\boldsymbol{O_B}, \boldsymbol{b}_1, \boldsymbol{b}_2, \boldsymbol{b}_3\}$ denotes the body-fixed frame, and $\boldsymbol{r}$ is the position of the UAV's center of mass relative to the origin $\boldsymbol{O_0}$.

reference is denoted by $\mathcal{N} = \{\boldsymbol{O_0}, \boldsymbol{n}_1, \boldsymbol{n}_2, \boldsymbol{n}_3\}$ and the body-fixed frame of reference, with its origin located at the flyer's center of mass, is denoted by $\mathcal{B} = \{\boldsymbol{O_B}, \boldsymbol{b}_1, \boldsymbol{b}_2, \boldsymbol{b}_3\}$. The globally-defined nonlinear dynamics of the system, including an LTV actuation dynamics, is represented as

$$m\ddot{\boldsymbol{r}} = -mg\boldsymbol{n}_3 + f_t\boldsymbol{b}_3, \tag{1}$$

$$\dot{\boldsymbol{q}} = \frac{1}{2}\boldsymbol{q} * \boldsymbol{p}, \tag{2}$$

$$\boldsymbol{J}\dot{\boldsymbol{\omega}} = -\boldsymbol{\omega} \times \boldsymbol{J}\boldsymbol{\omega} + \boldsymbol{\tau}, \tag{3}$$

$$\dot{\boldsymbol{\tau}} = -a(t)\boldsymbol{\tau} + b(t)\boldsymbol{u}, \tag{4}$$

where m is the mass of the vehicle; $\boldsymbol{J} = \text{diag}\{j_{11}, j_{22}, j_{33}\}$ is the moment of inertia matrix, written with respect to $\mathcal{B}$; $\boldsymbol{r}$ denotes the displacement of the UAV's center of mass from the origin of $\mathcal{N}$; f_t is the magnitude of the total thrust force generated by the UAV; $\boldsymbol{q}$ is the quaternion that represents the attitude of $\mathcal{B}$ with respect to $\mathcal{N}$; $\boldsymbol{p} = \begin{bmatrix}0 & \boldsymbol{\omega}^T\end{bmatrix}^T$; $\boldsymbol{\omega} = [\omega_1\ \omega_2\ \omega_3]^T$ is the angular velocity of the UAV with respect to $\mathcal{N}$ with its components expressed in $\mathcal{B}$; $\boldsymbol{\tau} = [\tau_1\ \tau_2\ \tau_3]^T$ is the torque generated by the propellers of the UAV; and, $\boldsymbol{u} = [u_1\ u_2\ u_3]^T$ is the control signal.

The aerodynamic effects affecting the actuator dynamics are described using (4), where the unknown time-varying parameters $a(t)$ and $b(t)$ represent the effects of time variations of torque latency and the aerodynamic coefficients of the propellers, respectively. By applying momentum theory analyses (Leishman, 2006) and considering experimental observations (Chen & Pérez-Arancibia, 2019), the coefficients $a(t)$ and $b(t)$ are modeled as

$$a(t) = \psi_1 + \psi_2\eta_1(\omega_a) + \psi_3\eta_2(\dot{\omega}_a) = \boldsymbol{\theta}_1^T\boldsymbol{\zeta}, \tag{5}$$

$$b(t) = \psi_4 + \psi_5\eta_1(\omega_a) + \psi_6\eta_2(\dot{\omega}_a) = \boldsymbol{\theta}_2^T\boldsymbol{\zeta}, \tag{6}$$

where $\boldsymbol{\theta}_1 = [\psi_1\ \psi_2\ \psi_3]^T$ and $\boldsymbol{\theta}_2 = [\ \psi_4\ \psi_5\ \psi_6]^T$ are vectors with unknown constant parameters; ω_a is the angular speed about the rotation axis used in a given aerobatic maneuver; and, $\boldsymbol{\zeta} = [1\ \eta_1(\omega_a)\ \eta_2(\dot{\omega}_a)]^T$, with

$$\eta_1(\omega_a) = \frac{\omega_a}{\sqrt{1+\sigma_1^{-2}\omega_a^2}}, \quad \eta_2(\dot{\omega}_a) = \frac{\dot{\omega}_a}{\sqrt{1+\sigma_2^{-2}\dot{\omega}_a^2}}, \tag{7}$$

where σ_1 and σ_2 are real positive constants. It is straightforward to see that $-\sigma_1 < \eta_1(\omega_a) < \sigma_1$ and $-\sigma_2 < \eta_2(\dot{\omega}_a) < \sigma_2$, for all ω_a and $\dot{\omega}_a$. Additionally, we enforce that $a(t) \geq a_{\min} > 0$ and $b(t) \geq b_{\min} > 0$, with $a_{\min}, b_{\min} \in \mathbb{R}$.

Overall, the model given by (4) is a simplification of the complex dynamic interactions of the UAV's propellers with the surrounding air flow that are generated during aerobatic flight. Consequently, this modeling approach is useful for controller synthesis while, to a significant extent, also allows us to capture the behavior of the aerodynamic effects influencing the controlled UAV. However, it is not expected to accurately describe the actual aerodynamic phenomena associated with the considered aerobatic flight problem.

3.2. Attitude-error kinematics

We define the ideal body frame, $\mathcal{I}$, as the desired rigid attitude kinematics required to follow the angular-velocity reference and that is initiated with zero attitude error. Accordingly,

$$\dot{\boldsymbol{q}}_d = \frac{1}{2}\boldsymbol{q}_d * \bar{\boldsymbol{p}}, \quad \text{with } \bar{\boldsymbol{p}} = \begin{bmatrix}0 & \bar{\boldsymbol{\omega}}_d^T\end{bmatrix}^T, \tag{8}$$

where $\boldsymbol{q}_d$ describes the attitude of $\mathcal{I}$. Since the desired angular velocity $\boldsymbol{\omega}_d$ is expressed in $\mathcal{B}$, not $\mathcal{I}$, we use the ideal angular velocity $\bar{\boldsymbol{\omega}}_d$ to specify (8), which has exactly the same components as $\boldsymbol{\omega}_d$ but is expressed in $\mathcal{I}$. Consistent with the quaternion-based description of the UAV's kinematics, the attitude control error is represented using the quaternion $\boldsymbol{q}_e$, which stores the information about the attitude difference between $\mathcal{B}$ and $\mathcal{I}$, and is given by

$$\boldsymbol{q}_e = \boldsymbol{q}_d^{-1} * \boldsymbol{q} = \begin{bmatrix} e_0 \\ \boldsymbol{e}_1 \end{bmatrix}. \tag{9}$$

Note that the vector part of $\boldsymbol{q}_e$, $\boldsymbol{e}_1$, and the scalar part of $\boldsymbol{q}_e$, e_0, contain the information about the Euler axis and rotation angle required to reach $\mathcal{I}$ from $\mathcal{B}$. Here, we denote this rotation angle by Θ_e, which by definition is always nonnegative and satisfies the quaternion identity $e_0 = \cos\frac{\Theta_e}{2}$. Last in this section, taking the time derivative of (9) along the trajectories of (2) and (8), we obtain that

$$\dot{\boldsymbol{q}}_e = \begin{bmatrix} \dot{e}_0 \\ \dot{\boldsymbol{e}}_1 \end{bmatrix} = \frac{1}{2}\begin{bmatrix} -\boldsymbol{e}_1^T[\boldsymbol{\omega} - \bar{\boldsymbol{\omega}}_d] \\ e_0[\boldsymbol{\omega} - \bar{\boldsymbol{\omega}}_d] + \boldsymbol{e}_1 \times [\boldsymbol{\omega} + \bar{\boldsymbol{\omega}}_d] \end{bmatrix}. \tag{10}$$

3.3. Control objectives

The main control objective is to compel the attitude and velocity dynamics of the controlled UAV, specified by (2) and (3), to track $\mathcal{I}$ and the angular-velocity reference $\boldsymbol{\omega}_d$ in the presence of the LTV actuator dynamics in (4) with the unknown time-varying parameters defined by (5) and (6). Due to the extremely short duration of an aerobatic maneuver (normally, less than one second) and its fast angular speed (with values as high as $2 \times 10^3\,^\circ \cdot s^{-1}$), it is more important to control the *faster* dynamics specified by (3) than the *slower* dynamics specified by (2). Consistently, the control objectives to be satisfied during an aerobatic maneuver are mathematically specified as

- The signals $\boldsymbol{\omega}, \boldsymbol{\tau} \in \mathcal{L}_\infty$.
- $\lim_{t\to\infty} \boldsymbol{e}_\omega(t) = \lim_{t\to\infty} [\boldsymbol{\omega}(t) - \boldsymbol{\omega}_d(t)] = \boldsymbol{0}$.
- Θ_e remains bounded during aerobatic flight.

For details about the definition of $\mathcal{L}_\infty$, see Ioannou and Fidan (2006).

4. Controller design and stability analysis

We present two different adaptive control methods to achieve the control objectives. The first method is a Lyapunov-based adaptive scheme, for which both the controller and adaptation law are derived using a single Lyapunov candidate function. The second method is a modular adaptive scheme, for which the controller and adaptation law are designed separately.

4.1. Lyapunov-based adaptive control

The chosen desired angular-velocity dynamics is given by $\boldsymbol{J}\dot{\boldsymbol{\omega}}_{\mathrm{d}} + \boldsymbol{\omega}_{\mathrm{d}} \times \boldsymbol{J}\boldsymbol{\omega}_{\mathrm{d}} = \boldsymbol{\tau}_{\mathrm{d}}$, where $\boldsymbol{\tau}_{\mathrm{d}}$ is the nominal torque required to achieve the desired dynamic behavior and $\boldsymbol{\omega}_{\mathrm{d}} = \begin{bmatrix}\omega_{\mathrm{d},1} & \omega_{\mathrm{d},2} & \omega_{\mathrm{d},3}\end{bmatrix}^T$ is the angular-velocity reference. For consistency and simplicity, $\boldsymbol{\omega}_{\mathrm{d}}, \boldsymbol{\tau}_{\mathrm{d}} \in \mathcal{L}_\infty$ and, additionally, $\boldsymbol{\omega}_{\mathrm{d}}$ satisfies the requirements in Definition 1. By defining $\boldsymbol{f}(\boldsymbol{\omega}) = \boldsymbol{\omega} \times \boldsymbol{J}\boldsymbol{\omega}$ and using its Taylor expansion, it can be shown that

$$\boldsymbol{f}(\boldsymbol{\omega}) = \boldsymbol{f}(\boldsymbol{\omega}_{\mathrm{d}}) + \boldsymbol{D}_{\boldsymbol{f}}(\boldsymbol{\omega}_{\mathrm{d}})\boldsymbol{e}_{\boldsymbol{\omega}} + \boldsymbol{g}(t, \boldsymbol{\omega}), \tag{11}$$

where $\boldsymbol{D}_{\boldsymbol{f}}(\boldsymbol{\omega}_{\mathrm{d}}) = \frac{\partial \boldsymbol{f}(\boldsymbol{\omega})}{\partial \boldsymbol{\omega}}\Big|_{\boldsymbol{\omega}=\boldsymbol{\omega}_{\mathrm{d}}}$; $\boldsymbol{e}_{\boldsymbol{\omega}} = \boldsymbol{\omega} - \boldsymbol{\omega}_{\mathrm{d}}$; and, $\boldsymbol{g}(t, \boldsymbol{\omega})$ is the high-order nonlinear residue of the expansion and has the compact form $\boldsymbol{g}(t, \boldsymbol{\omega}) = \boldsymbol{h}(\boldsymbol{e}_{\boldsymbol{\omega}}) = \boldsymbol{e}_{\boldsymbol{\omega}} \times \boldsymbol{J}\boldsymbol{e}_{\boldsymbol{\omega}}$. Then, by subtracting the desired angular-velocity dynamics from (3), we obtain that

$$\boldsymbol{J}\dot{\boldsymbol{e}}_{\boldsymbol{\omega}} + \boldsymbol{D}_{\boldsymbol{f}}(\boldsymbol{\omega}_{\mathrm{d}})\boldsymbol{e}_{\boldsymbol{\omega}} + \boldsymbol{h}(\boldsymbol{e}_{\boldsymbol{\omega}}) = \boldsymbol{\tau} - \boldsymbol{\tau}_{\mathrm{d}}. \tag{12}$$

The method discussed in this section requires the definition of a virtual torque input for (3). For this purpose, we utilize the LTI controller in Chen and Pérez-Arancibia (2017, 2020), which was designed using the nominal dynamics of the controlled UAV without considering the time-varying actuation dynamics of the system. This LTI controller has the form

$$\boldsymbol{\tau}_{\mathrm{a}} = -\boldsymbol{K}_1\boldsymbol{e}_{\boldsymbol{\omega}} + \boldsymbol{v} + \boldsymbol{\tau}_{\mathrm{d}}, \tag{13}$$

$$\dot{\boldsymbol{v}} = -\lambda\boldsymbol{v} + \boldsymbol{K}_2\boldsymbol{e}_{\boldsymbol{\omega}}, \tag{14}$$

where $\boldsymbol{K}_1$ and $\boldsymbol{K}_2$ are diagonal positive-definite matrices that satisfy the condition that $\lambda\boldsymbol{K}_1 \succ \boldsymbol{K}_2$, for $0 < \lambda \in \mathbb{R}$. The estimated vector parameters are denoted by $\hat{\boldsymbol{\theta}}_1$ and $\hat{\boldsymbol{\theta}}_2$, and the estimation errors are defined as $\tilde{\boldsymbol{\theta}}_1 = \boldsymbol{\theta}_1 - \hat{\boldsymbol{\theta}}_1$ and $\tilde{\boldsymbol{\theta}}_2 = \boldsymbol{\theta}_2 - \hat{\boldsymbol{\theta}}_2$. The *proto*-Lyapunov function used for controller synthesis is selected to be

$$\begin{aligned} V_1 = {} & \frac{1}{2}\boldsymbol{e}_{\boldsymbol{\omega}}^T\boldsymbol{J}\boldsymbol{e}_{\boldsymbol{\omega}} + \frac{1}{2}\boldsymbol{v}^T\boldsymbol{Q}_1\boldsymbol{v} + \frac{1}{2}[\boldsymbol{\tau} - \boldsymbol{\tau}_{\mathrm{a}}]^T\boldsymbol{Q}_2[\boldsymbol{\tau} - \boldsymbol{\tau}_{\mathrm{a}}] \\ & + \frac{1}{2}\tilde{\boldsymbol{\theta}}_1^T\boldsymbol{K}_{\tilde{\boldsymbol{\theta}}_1}^{-1}\tilde{\boldsymbol{\theta}}_1 + \frac{1}{2}\tilde{\boldsymbol{\theta}}_2^T\boldsymbol{K}_{\tilde{\boldsymbol{\theta}}_2}^{-1}\tilde{\boldsymbol{\theta}}_2, \end{aligned} \tag{15}$$

where $\boldsymbol{Q}_1$, $\boldsymbol{Q}_2$, $\boldsymbol{K}_{\tilde{\boldsymbol{\theta}}_1}$, and $\boldsymbol{K}_{\tilde{\boldsymbol{\theta}}_2}$ are diagonal positive-definite matrices. Then, by taking the time derivative of V_1 along the trajectories specified by (12) and (14), and substituting the virtual control input defined by (13) into the result, we obtain

$$\begin{aligned} \dot{V}_1 = {} & -\begin{bmatrix}\boldsymbol{e}_{\boldsymbol{\omega}}^T & \boldsymbol{v}^T\end{bmatrix}\boldsymbol{G}(t)\begin{bmatrix}\boldsymbol{e}_{\boldsymbol{\omega}} \\ \boldsymbol{v}\end{bmatrix} + \boldsymbol{e}_{\boldsymbol{\omega}}^T[\boldsymbol{\tau} - \boldsymbol{\tau}_{\mathrm{a}}] \\ & + [\boldsymbol{\tau} - \boldsymbol{\tau}_{\mathrm{a}}]^T\boldsymbol{Q}_2\big[-a(t)\boldsymbol{\tau} + b(t)\boldsymbol{u} - \dot{\boldsymbol{\tau}}_{\mathrm{a}}\big] \\ & - \tilde{\boldsymbol{\theta}}_1^T\boldsymbol{K}_{\tilde{\boldsymbol{\theta}}_1}^{-1}\dot{\hat{\boldsymbol{\theta}}}_1 - \tilde{\boldsymbol{\theta}}_2^T\boldsymbol{K}_{\tilde{\boldsymbol{\theta}}_2}^{-1}\dot{\hat{\boldsymbol{\theta}}}_2, \end{aligned} \tag{16}$$

where

$$\boldsymbol{G}(t) = \begin{bmatrix} \boldsymbol{K}_1 + \frac{1}{2}\big[\boldsymbol{D}_{\boldsymbol{f}}(\boldsymbol{\omega}_{\mathrm{d}}) + \boldsymbol{D}_{\boldsymbol{f}}^T(\boldsymbol{\omega}_{\mathrm{d}})\big] & -\frac{1}{2}\big[\boldsymbol{I} + \boldsymbol{K}_2^T\boldsymbol{Q}_1^T\big] \\ -\frac{1}{2}[\boldsymbol{I} + \boldsymbol{Q}_1\boldsymbol{K}_2] & \lambda\boldsymbol{Q}_1 \end{bmatrix}. \tag{17}$$

It is immediately clear that one of the closed-loop stability conditions is that $\boldsymbol{G}(t) \succ 0$, for all $t \geq t_0$. In Chen and Pérez-Arancibia (2020), we show that $\boldsymbol{G}(t)$ remains in a convex hull defined by two constant symmetric matrices, $\boldsymbol{G}_1$ and $\boldsymbol{G}_2$. Therein, we also show that the condition that $\boldsymbol{G}(t) \succ 0$ is equivalent to satisfying that $\boldsymbol{G}_1 \succ 0$ and $\boldsymbol{G}_2 \succ 0$. Finding parameters $\boldsymbol{K}_1$, $\boldsymbol{K}_2$, and λ that enforce the conditions $\boldsymbol{G}_1 \succ 0$ and $\boldsymbol{G}_2 \succ 0$ is a semidefinite programming problem that can always be solved (Boyd & Vandenberghe, 2004).

The control input $\boldsymbol{u}$ is chosen to have the form

$$\boldsymbol{u} = \hat{b}^{-1}(t)\big[\hat{a}(t)\boldsymbol{\tau} + \dot{\boldsymbol{\tau}}_{\mathrm{a}} - \boldsymbol{Q}_2^{-1}\boldsymbol{e}_{\boldsymbol{\omega}} - \boldsymbol{K}_3[\boldsymbol{\tau} - \boldsymbol{\tau}_{\mathrm{a}}]\big], \tag{18}$$

where $\boldsymbol{K}_3$ is a diagonal positive-definite gain matrix; $\hat{b}(t)$ is an estimation of $b(t)$ with the form $\hat{b} = \hat{\psi}_4 + \hat{\psi}_5\eta_1(\omega_{\mathrm{a}}) + \hat{\psi}_6\eta_2(\dot{\omega}_{\mathrm{a}})$; and, $\hat{a}(t)$ is an estimation of the parameter $a(t)$ with the form $\hat{a} = \hat{\psi}_1 + \hat{\psi}_2\eta_1(\omega_{\mathrm{a}}) + \hat{\psi}_3\eta_2(\dot{\omega}_{\mathrm{a}})$. The estimation errors are defined as $\tilde{a}(t) = a(t) - \hat{a}(t) = \tilde{\boldsymbol{\theta}}_1^T(t)\boldsymbol{\zeta}(t)$ and $\tilde{b}(t) = b(t) - \hat{b}(t) = \tilde{\boldsymbol{\theta}}_2^T(t)\boldsymbol{\zeta}(t)$. Then, by substituting the control input specified by (18) into (16), we obtain that

$$\begin{aligned} \dot{V}_1 = {} & -\begin{bmatrix}\boldsymbol{e}_{\boldsymbol{\omega}}^T & \boldsymbol{v}^T\end{bmatrix}\boldsymbol{G}(t)\begin{bmatrix}\boldsymbol{e}_{\boldsymbol{\omega}} \\ \boldsymbol{v}\end{bmatrix} - [\boldsymbol{\tau} - \boldsymbol{\tau}_{\mathrm{a}}]^T\boldsymbol{Q}_2\boldsymbol{K}_3[\boldsymbol{\tau} - \boldsymbol{\tau}_{\mathrm{a}}] \\ & - \tilde{\boldsymbol{\theta}}_1^T\left[\boldsymbol{\zeta}[\boldsymbol{\tau} - \boldsymbol{\tau}_{\mathrm{a}}]^T\boldsymbol{Q}_2\boldsymbol{\tau} + \boldsymbol{K}_{\tilde{\boldsymbol{\theta}}_1}^{-1}\dot{\hat{\boldsymbol{\theta}}}_1\right] \\ & + \tilde{\boldsymbol{\theta}}_2^T\left[\boldsymbol{\zeta}[\boldsymbol{\tau} - \boldsymbol{\tau}_{\mathrm{a}}]^T\boldsymbol{Q}_2\boldsymbol{u} - \boldsymbol{K}_{\tilde{\boldsymbol{\theta}}_2}^{-1}\dot{\hat{\boldsymbol{\theta}}}_2\right]. \end{aligned} \tag{19}$$

The estimates $\hat{a}(t)$ and $\hat{b}(t)$ must satisfy that $\hat{a}(t) \geq a_{\min}$ and $\hat{b}(t) \geq b_{\min}$, for the real positive constants $a_{\min}$ and $b_{\min}$. To enforce these conditions, the parameters $\{\hat{\psi}_1, \hat{\psi}_2, \hat{\psi}_3, \hat{\psi}_4, \hat{\psi}_5, \hat{\psi}_6\}$ are set to be bounded according to the rules

$$\gamma_{\min,1} \leq \hat{\psi}_1 \leq \gamma_{\max,1}, \quad -\gamma_2 \leq \hat{\psi}_2 \leq \gamma_2, \quad -\gamma_3 \leq \hat{\psi}_3 \leq \gamma_3, \tag{20}$$

$$\gamma_{\min,4} \leq \hat{\psi}_4 \leq \gamma_{\max,4}, \quad -\gamma_5 \leq \hat{\psi}_5 \leq \gamma_5, \quad -\gamma_6 \leq \hat{\psi}_6 \leq \gamma_6, \tag{21}$$

where, $\gamma_{\min,1}$, $\gamma_{\max,1}$, γ_2, γ_3, $\gamma_{\min,4}$, $\gamma_{\max,4}$, γ_5, and γ_6 are real positive constants; the relationships $\gamma_{\min,1} - \sigma_1\gamma_2 - \sigma_2\gamma_3 \geq a_{\min}$ and $\gamma_{\min,4} - \sigma_1\gamma_5 - \sigma_2\gamma_6 \geq b_{\min}$ must also be satisfied. In this case, we apply the parameter projection algorithm (Ioannou & Fidan, 2006; Ioannou & Sun, 2012) to ensure that $\hat{\boldsymbol{\theta}}_1$ and $\hat{\boldsymbol{\theta}}_2$ generate the conditions specified by (20) and (21). Accordingly, two convex sets are defined, $\mathcal{S}_1 = \{\hat{\boldsymbol{\theta}}_1 \in \mathbb{R}^3 \mid g_1(\hat{\boldsymbol{\theta}}_1) \leq 0\}$ and $\mathcal{S}_2 = \{\hat{\boldsymbol{\theta}}_2 \in \mathbb{R}^3 \mid g_2(\hat{\boldsymbol{\theta}}_2) \leq 0\}$, where

$$g_1(\hat{\boldsymbol{\theta}}_1) = \left(\frac{2\hat{\psi}_1 - \gamma_{\min,1} - \gamma_{\max,1}}{\gamma_{\max,1} - \gamma_{\min,1}}\right)^{2n} + \left(\frac{\hat{\psi}_2}{\gamma_2}\right)^{2n} + \left(\frac{\hat{\psi}_3}{\gamma_3}\right)^{2n} - 1, \tag{22}$$

$$g_2(\hat{\boldsymbol{\theta}}_2) = \left(\frac{2\hat{\psi}_4 - \gamma_{\min,4} - \gamma_{\max,4}}{\gamma_{\max,4} - \gamma_{\min,4}}\right)^{2n} + \left(\frac{\hat{\psi}_5}{\gamma_5}\right)^{2n} + \left(\frac{\hat{\psi}_6}{\gamma_6}\right)^{2n} - 1, \tag{23}$$

and n can be chosen to be any positive integer.

Consistently, the resulting adaptation laws used to compute $\hat{\boldsymbol{\theta}}_1$ and $\hat{\boldsymbol{\theta}}_2$ are specified by

$$\dot{\hat{\boldsymbol{\theta}}}_1 = \begin{cases} \boldsymbol{\xi}_1, \text{ if } \hat{\boldsymbol{\theta}}_1 \in \mathring{\mathcal{S}}_1, \text{ or if } \hat{\boldsymbol{\theta}}_1 \in \partial\mathcal{S}_1 \text{ and } \nabla g_1^T\boldsymbol{\xi}_1 \leq 0; \\ \boldsymbol{\xi}_1 - \boldsymbol{K}_{\tilde{\boldsymbol{\theta}}_1}\frac{\nabla g_1 \nabla g_1^T}{\nabla g_1^T\boldsymbol{K}_{\tilde{\boldsymbol{\theta}}_1}\nabla g_1}\boldsymbol{\xi}_1, \qquad \text{otherwise.} \end{cases} \tag{24}$$

$$\dot{\hat{\boldsymbol{\theta}}}_2 = \begin{cases} \boldsymbol{\xi}_2, \text{ if } \hat{\boldsymbol{\theta}}_2 \in \mathring{\mathcal{S}}_2, \text{ or if } \hat{\boldsymbol{\theta}}_2 \in \partial\mathcal{S}_2 \text{ and } \nabla g_2^T\boldsymbol{\xi}_2 \leq 0; \\ \boldsymbol{\xi}_2 - \boldsymbol{K}_{\tilde{\boldsymbol{\theta}}_2}\frac{\nabla g_2 \nabla g_2^T}{\nabla g_2^T\boldsymbol{K}_{\tilde{\boldsymbol{\theta}}_2}\nabla g_2}\boldsymbol{\xi}_2, \qquad \text{otherwise.} \end{cases} \tag{25}$$

The variables used in the computation of the projections are defined as $\boldsymbol{\xi}_1 = -\boldsymbol{K}_{\tilde{\boldsymbol{\theta}}_1}\boldsymbol{\zeta}[\boldsymbol{\tau} - \boldsymbol{\tau}_{\mathrm{a}}]^T\boldsymbol{Q}_2\boldsymbol{\tau}$ and $\boldsymbol{\xi}_2 = \boldsymbol{K}_{\tilde{\boldsymbol{\theta}}_2}\boldsymbol{\zeta}[\boldsymbol{\tau} - \boldsymbol{\tau}_{\mathrm{a}}]^T\boldsymbol{Q}_2\boldsymbol{u}$. Note that when $\dot{\hat{\boldsymbol{\theta}}}_1 = \boldsymbol{\xi}_1$ and $\dot{\hat{\boldsymbol{\theta}}}_2 = \boldsymbol{\xi}_2$, $\dot{V}_1$ is negative definite, with the form

$$\dot{V}_1 = -\begin{bmatrix}\boldsymbol{e}_{\boldsymbol{\omega}}^T & \boldsymbol{v}^T\end{bmatrix}\boldsymbol{G}(t)\begin{bmatrix}\boldsymbol{e}_{\boldsymbol{\omega}} \\ \boldsymbol{v}\end{bmatrix} - [\boldsymbol{\tau} - \boldsymbol{\tau}_{\mathrm{a}}]^T\boldsymbol{Q}_2\boldsymbol{K}_3[\boldsymbol{\tau} - \boldsymbol{\tau}_{\mathrm{a}}]. \tag{26}$$

Thus, considering that V_1 is positive definite and $\dot{V}_1 \leq 0$, it follows that $V_1 \in \mathcal{L}_\infty$, which implies that $\boldsymbol{e}_{\boldsymbol{\omega}}$, $\boldsymbol{v}$, and $[\boldsymbol{\tau} - \boldsymbol{\tau}_{\mathrm{a}}] \in \mathcal{L}_\infty$. Also,

integrating both sides of (26), we obtain that

$$\begin{aligned}&\min_t\{\lambda_{\min}\{\boldsymbol{G}(t)\}\}\int_{t_0}^{\infty}\left(|\boldsymbol{e}_{\boldsymbol{\omega}}|_2^2+|\boldsymbol{v}|_2^2\right)d\tau\\&+\lambda_{\min}\{\boldsymbol{Q}_2\boldsymbol{K}_3\}\int_{t_0}^{\infty}|\boldsymbol{\tau}-\boldsymbol{\tau}_{\mathrm{a}}|_2^2\,d\tau\leq V_1(t_0)-V_1(\infty).\end{aligned}\tag{27}$$

Because $V_1(t_0)$ and $V_1(\infty)$ are bounded, we can also conclude that $\boldsymbol{e}_{\boldsymbol{\omega}}$, $\boldsymbol{v}$, and $[\boldsymbol{\tau}-\boldsymbol{\tau}_{\mathrm{a}}]\in\mathcal{L}_2$, and from (4), (12), (13), (14), and (18), it follows that $\dot{\boldsymbol{e}}_{\boldsymbol{\omega}}$, $\dot{\boldsymbol{v}}$, and $\left[\dot{\boldsymbol{\tau}}-\dot{\boldsymbol{\tau}}_{\mathrm{a}}\right]\in\mathcal{L}_\infty$. Furthermore, using Barbalat's lemma, we can prove that $\boldsymbol{e}_{\boldsymbol{\omega}}$, $\boldsymbol{v}$, and $[\boldsymbol{\tau}-\boldsymbol{\tau}_{\mathrm{a}}]$ converge to zero asymptotically, which guarantees the stability of the closed-loop adaptive system.

Lastly in this section, when the parameters $\hat{\boldsymbol{\theta}}_1\in\partial\mathcal{S}_1$ with $\nabla g_1^T\boldsymbol{\xi}_1>0$ and $\hat{\boldsymbol{\theta}}_2\in\partial\mathcal{S}_2$ with $\nabla g_2^T\boldsymbol{\xi}_2>0$, it can be shown that

$$\begin{aligned}\dot{V}_1=&-\left[\boldsymbol{e}_{\boldsymbol{\omega}}^T\;\boldsymbol{v}^T\right]\boldsymbol{G}(t)\begin{bmatrix}\boldsymbol{e}_{\boldsymbol{\omega}}\\\boldsymbol{v}\end{bmatrix}-[\boldsymbol{\tau}-\boldsymbol{\tau}_{\mathrm{a}}]^T\boldsymbol{Q}_2\boldsymbol{K}_3[\boldsymbol{\tau}-\boldsymbol{\tau}_{\mathrm{a}}]\\&+\tilde{\boldsymbol{\theta}}_1^T\frac{\nabla g_1\nabla g_1^T}{\nabla g_1^T\boldsymbol{K}_{\tilde{\boldsymbol{\theta}}_1}\nabla g_1}\boldsymbol{\xi}_1+\tilde{\boldsymbol{\theta}}_2^T\frac{\nabla g_2\nabla g_2^T}{\nabla g_2^T\boldsymbol{K}_{\tilde{\boldsymbol{\theta}}_2}\nabla g_2}\boldsymbol{\xi}_2,\end{aligned}\tag{28}$$

which, considering that $\tilde{\boldsymbol{\theta}}_1^T\nabla g_1<0$ and $\tilde{\boldsymbol{\theta}}_2^T\nabla g_2<0$, implies that

$$\dot{V}_1\leq-\left[\boldsymbol{e}_{\boldsymbol{\omega}}^T\;\boldsymbol{v}^T\right]\boldsymbol{G}(t)\begin{bmatrix}\boldsymbol{e}_{\boldsymbol{\omega}}\\\boldsymbol{v}\end{bmatrix}-[\boldsymbol{\tau}-\boldsymbol{\tau}_{\mathrm{a}}]^T\boldsymbol{Q}_2\boldsymbol{K}_3[\boldsymbol{\tau}-\boldsymbol{\tau}_{\mathrm{a}}],\tag{29}$$

and, as a consequence, that $\dot{V}_1\leq0$. Then, using Barbalat's lemma one more time, it can be shown that $\boldsymbol{e}_{\boldsymbol{\omega}}$, $\boldsymbol{v}$, and $[\boldsymbol{\tau}-\boldsymbol{\tau}_{\mathrm{a}}]$ converge to zero asymptotically. Therefore, we conclude that the controller specified by (18), with the adaptation laws given by (24) and (25), generates a stable closed-loop angular-velocity error dynamics and the tracking error $\boldsymbol{e}_{\boldsymbol{\omega}}$ globally converges to zero asymptotically.

4.2. Modular adaptive control

The adaptation law that we used to define the Lyapunov-based adaptive scheme is constrained by the structure of the associated Lyapunov function. To remove this limitation, we propose a modular adaptive control scheme in which the adaptation law can be designed independently from the controller synthesis process. In this case, the first step is to synthesize a controller that guarantees that the closed-loop system is *input-to-state stable* (ISS) from the multivariable estimation error to the system state.

As explained in Sections 3.1 and 4.1, the open-loop system can be described as

$$\boldsymbol{J}\dot{\boldsymbol{e}}_{\boldsymbol{\omega}}+\boldsymbol{D}_{\boldsymbol{f}}(\boldsymbol{\omega}_{\mathrm{d}})\boldsymbol{e}_{\boldsymbol{\omega}}+\boldsymbol{h}(\boldsymbol{e}_{\boldsymbol{\omega}})=\boldsymbol{\tau}-\boldsymbol{\tau}_{\mathrm{d}},\tag{30}$$

$$\dot{\boldsymbol{\tau}}=-a(t)\boldsymbol{\tau}+b(t)\boldsymbol{u}.\tag{31}$$

Next, we define a *proto*-Lyapunov function with the form

$$V_2=\frac{1}{2}\boldsymbol{e}_{\boldsymbol{\omega}}^T\boldsymbol{J}\boldsymbol{e}_{\boldsymbol{\omega}}+\frac{1}{2}\boldsymbol{v}^T\boldsymbol{Q}_1\boldsymbol{v}+\frac{1}{2}[\boldsymbol{\tau}-\boldsymbol{\tau}_{\mathrm{a}}]^T\boldsymbol{Q}_3[\boldsymbol{\tau}-\boldsymbol{\tau}_{\mathrm{a}}],\tag{32}$$

where $\boldsymbol{Q}_1\succ\boldsymbol{0}$ and $\boldsymbol{Q}_3=q_3\boldsymbol{I}\succ\boldsymbol{0}$. Then, by taking the time derivative of V_2 along the trajectories specified by (30) and (31), and substituting the virtual torque given by (13) and (14) into the result, we obtain

$$\begin{aligned}\dot{V}_2=&-\left[\boldsymbol{e}_{\boldsymbol{\omega}}^T\;\boldsymbol{v}^T\right]\boldsymbol{G}(t)\begin{bmatrix}\boldsymbol{e}_{\boldsymbol{\omega}}\\\boldsymbol{v}\end{bmatrix}+\boldsymbol{e}_{\boldsymbol{\omega}}^T[\boldsymbol{\tau}-\boldsymbol{\tau}_{\mathrm{a}}]\\&+[\boldsymbol{\tau}-\boldsymbol{\tau}_{\mathrm{a}}]^T\boldsymbol{Q}_3\left[-a(t)\boldsymbol{\tau}+b(t)\boldsymbol{u}-\dot{\boldsymbol{\tau}}_{\mathrm{a}}\right].\end{aligned}\tag{33}$$

Furthermore, we define the control input to be

$$\begin{aligned}\boldsymbol{u}=&\hat{b}^{-1}(t)\boldsymbol{\phi}+\frac{\operatorname{sgn}\{b(t)\}}{b_{\min}}\Big[-\boldsymbol{\tau}\boldsymbol{\tau}^T\boldsymbol{Q}_3[\boldsymbol{\tau}-\boldsymbol{\tau}_{\mathrm{a}}]\\&-\hat{b}^{-2}(t)\boldsymbol{\phi}\boldsymbol{\phi}^T\boldsymbol{Q}_3[\boldsymbol{\tau}-\boldsymbol{\tau}_{\mathrm{a}}]\Big],\end{aligned}\tag{34}$$

where

$$\boldsymbol{\phi}=\hat{a}(t)\boldsymbol{\tau}+\dot{\boldsymbol{\tau}}_{\mathrm{a}}-\boldsymbol{K}_4[\boldsymbol{\tau}-\boldsymbol{\tau}_{\mathrm{a}}]\tag{35}$$

and $\boldsymbol{K}_4$ is a diagonal positive-definite matrix. Then, noting that $\frac{b(t)}{b_{\min}}\geq1$, defining $\boldsymbol{z}=\boldsymbol{\tau}-\boldsymbol{\tau}_{\mathrm{a}}$, substituting the control input specified by (34) into (33), and defining $\boldsymbol{x}=\left[\boldsymbol{e}_{\boldsymbol{\omega}}^T\;\boldsymbol{v}^T\;\boldsymbol{z}^T\right]^T$, we arrive at

$$\begin{aligned}\dot{V}_2\leq&-\boldsymbol{x}^T\boldsymbol{H}(t)\boldsymbol{x}-\left(\boldsymbol{\tau}^T\boldsymbol{Q}_3\boldsymbol{z}+\frac{\tilde{a}(t)}{2}\right)^2\\&-\left(\hat{b}^{-1}(t)\boldsymbol{\phi}^T\boldsymbol{Q}_3\boldsymbol{z}-\frac{\tilde{b}(t)}{2}\right)^2+\frac{\tilde{a}^2(t)}{4}+\frac{\tilde{b}^2(t)}{4},\end{aligned}\tag{36}$$

and consequently, we further deduce that

$$\dot{V}_2\leq-\boldsymbol{x}^T\boldsymbol{H}(t)\boldsymbol{x}+\frac{\tilde{a}^2(t)}{4}+\frac{\tilde{b}^2(t)}{4},\tag{37}$$

where

$$\boldsymbol{H}(t)=\left[\begin{array}{cc|c}\multicolumn{2}{c|}{\multirow{2}{*}{$\boldsymbol{G}(t)$}}&-\frac{1}{2}\boldsymbol{I}_{3\times3}\\&&\boldsymbol{0}_{3\times3}\\\hline-\frac{1}{2}\boldsymbol{I}_{3\times3}&\boldsymbol{0}_{3\times3}&\boldsymbol{Q}_3\boldsymbol{K}_4\end{array}\right];\tag{38}$$

$\tilde{a}(t)=a(t)-\hat{a}(t)$; and, $\tilde{b}(t)=b(t)-\hat{b}(t)$.

It is clear that one of the stability conditions is that $\boldsymbol{H}(t)\succ0$, for all $t\geq t_0$. Also, similarly to the case of $\boldsymbol{G}(t)$, given the properties of $\boldsymbol{H}(t)$, it can be shown that $\boldsymbol{H}(t)$ remains in a convex hull defined by two constant matrices. Therefore, for given matrices $\boldsymbol{Q}_1$ and $\boldsymbol{Q}_3$, and the signal $\boldsymbol{\omega}_{\mathrm{d}}(t)$, the problem of finding the controller parameters $\boldsymbol{K}_1$, $\boldsymbol{K}_2$, $\boldsymbol{K}_4$, and λ to satisfy the condition that $\boldsymbol{H}(t)\succ\boldsymbol{0}$ is a semidefinite programming problem that can always be solved.

Proposition 1. *Given matrices $\boldsymbol{Q}_1\succ\boldsymbol{0}$, $\boldsymbol{Q}_3\succ\boldsymbol{0}$, and $\boldsymbol{H}(t)\succ\boldsymbol{0}$, for all $t\geq t_0$, the system specified by (30) and (31), with the control input in (34), is ISS with respect to $\left\{\tilde{a}(t),\tilde{b}(t)\right\}$, for all $t\geq t_0$.*

Proof. See Appendix A.1. □

The conditions stated in Proposition 1 ensure that the system state, $\{\boldsymbol{e}_{\boldsymbol{\omega}},\boldsymbol{v},\boldsymbol{z}\}$, remains bounded provided that the estimation errors $\tilde{a}(t)$ and $\tilde{b}(t)$ remain bounded. Additionally, from (5) and (6), it is straightforward to see that $\tilde{a}(t)$ and $\tilde{b}(t)$ are bounded as long as $\tilde{\boldsymbol{\theta}}_1(t)$ and $\tilde{\boldsymbol{\theta}}_2(t)$ remain bounded. Next, we design the adaptation law for the control scheme. First, we substitute the control input specified by (34) into (4), which yields

$$\dot{\boldsymbol{z}}=\boldsymbol{A}_{\boldsymbol{z}}(t)\boldsymbol{z}+\boldsymbol{W}^T(t)\tilde{\boldsymbol{\theta}}(t),\tag{39}$$

where

$$\tilde{\boldsymbol{\theta}}=\left[\tilde{\boldsymbol{\theta}}_1^T\;\tilde{\boldsymbol{\theta}}_2^T\right]^T;\tag{40}$$

$$\boldsymbol{A}_{\boldsymbol{z}}=-\left[\boldsymbol{K}_4+\frac{\hat{b}\operatorname{sgn}\{b\}q_3}{b_{\min}}\left[\boldsymbol{\tau}\boldsymbol{\tau}^T+\hat{b}^{-2}\boldsymbol{\phi}\boldsymbol{\phi}^T\right]\right];\tag{41}$$

$$\boldsymbol{W}^T=\left[-\boldsymbol{\tau}\boldsymbol{\zeta}^T\quad\left[\frac{\operatorname{sgn}\{b\}q_3}{b_{\min}}\left[-\boldsymbol{\tau}\boldsymbol{\tau}^T-\hat{b}^{-2}\boldsymbol{\phi}\boldsymbol{\phi}^T\right]\boldsymbol{z}+\hat{b}^{-1}\boldsymbol{\phi}\right]\boldsymbol{\zeta}^T\right].\tag{42}$$

It is straightforward to see that $\boldsymbol{A}_{\boldsymbol{z}}(t)$ is exponentially stable[5] because $\boldsymbol{K}_4$ is positive definite and $\frac{\hat{b}\operatorname{sgn}\{b\}q_3}{b_{\min}}\left[\boldsymbol{\tau}\boldsymbol{\tau}^T+\hat{b}^{-2}\boldsymbol{\phi}\boldsymbol{\phi}^T\right]$ is positive semidefinite as long as $\hat{b}(t)$ is guaranteed to remain positive using parameter projection.

[5] This means that there exists a positive-definite symmetric matrix $\boldsymbol{R}$ such that $\boldsymbol{R}\boldsymbol{A}_{\boldsymbol{z}}(t)+\boldsymbol{A}_{\boldsymbol{z}}^T(t)\boldsymbol{R}\prec0$, for all $t\geq t_0$.

Then, applying the *nonlinear swapping lemma* (Krstić et al., 1995) to rearrange (39), we obtain the filters

$$\dot{\boldsymbol{\Gamma}}^T = \boldsymbol{A}_{\boldsymbol{z}}\boldsymbol{\Gamma}^T + \boldsymbol{W}^T, \tag{43}$$

$$\dot{\boldsymbol{\mu}} = \boldsymbol{A}_{\boldsymbol{z}}\boldsymbol{\mu} + \boldsymbol{W}^T\hat{\boldsymbol{\theta}}, \tag{44}$$

where $\hat{\boldsymbol{\theta}} = \begin{bmatrix}\hat{\boldsymbol{\theta}}_1^T & \hat{\boldsymbol{\theta}}_2^T\end{bmatrix}^T$. In this way, using (39), (43), and (44), we derive the static linear parametric model

$$\boldsymbol{z} + \boldsymbol{\mu} = \boldsymbol{\Gamma}^T\boldsymbol{\theta} + \tilde{\boldsymbol{\varepsilon}}, \tag{45}$$

where $\tilde{\boldsymbol{\varepsilon}}$ is governed by the dynamics $\dot{\tilde{\boldsymbol{\varepsilon}}} = \boldsymbol{A}_{\boldsymbol{z}}\tilde{\boldsymbol{\varepsilon}}$, which implies that $\tilde{\boldsymbol{\varepsilon}}$ decays to zero exponentially fast and $\tilde{\boldsymbol{\varepsilon}} \in \mathcal{L}_\infty \cap \mathcal{L}_2$ because $\boldsymbol{A}_{\boldsymbol{z}}$ is exponentially stable. Then, putting everything together, we obtain an expression for the prediction error, $\boldsymbol{\varepsilon}$, with the form

$$\boldsymbol{\Gamma}^T\boldsymbol{\theta} + \tilde{\boldsymbol{\varepsilon}} - \boldsymbol{\Gamma}^T\hat{\boldsymbol{\theta}} = \boldsymbol{\Gamma}^T\tilde{\boldsymbol{\theta}} + \tilde{\boldsymbol{\varepsilon}} = \boldsymbol{z} + \boldsymbol{\mu} - \boldsymbol{\Gamma}^T\hat{\boldsymbol{\theta}} = \boldsymbol{\varepsilon}. \tag{46}$$

Since the estimation error $\boldsymbol{\varepsilon}$ is linear in $\tilde{\boldsymbol{\theta}}$, we can use any gradient algorithm or the least-squares method to estimate $\boldsymbol{\theta}$. In this case, we use the *recursive least-squares* (RLS) algorithm as stated in Ioannou and Sun (2012). Namely,

$$\dot{\hat{\boldsymbol{\theta}}} = \text{Proj}\{\boldsymbol{\varrho}\} = \text{Proj}\left\{\boldsymbol{P}\frac{\boldsymbol{\Gamma}\boldsymbol{\varepsilon}}{1+\nu\,\text{tr}\{\boldsymbol{\Gamma}^T\boldsymbol{P}\boldsymbol{\Gamma}\}}\right\}, \tag{47}$$

$$\dot{\boldsymbol{P}} = \begin{cases} \beta\boldsymbol{P} - \dfrac{\boldsymbol{P}\boldsymbol{\Gamma}\boldsymbol{\Gamma}^T\boldsymbol{P}}{1+\nu\,\text{tr}\{\boldsymbol{\Gamma}^T\boldsymbol{P}\boldsymbol{\Gamma}\}}, & \text{if } \|\boldsymbol{P}\|_{\text{F}} \le P_{\max}; \\ \boldsymbol{0}, & \text{otherwise.} \end{cases} \tag{48}$$

The parameters β, ν, and $P_{\max}$ are real positive constants, and $\text{Proj}\{\cdot\}$ denotes the projection operator in Krstić et al. (1995) given by

$$\text{Proj}\{\boldsymbol{\varrho}\} = \begin{cases} \boldsymbol{\varrho}, & \text{if } \hat{\boldsymbol{\theta}} \in \mathring{\mathcal{S}}_{\text{m}} \text{ or } \nabla g_{\text{m}}^T\boldsymbol{\varrho} \le 0; \\ \left[\boldsymbol{I} - c(\hat{\boldsymbol{\theta}})\boldsymbol{K}_{\text{m}}\dfrac{\nabla g_{\text{m}}\nabla g_{\text{m}}^T}{\nabla g_{\text{m}}^T\boldsymbol{K}_{\text{m}}\nabla g_{\text{m}}}\right]\boldsymbol{\varrho}, & \\ \quad \text{if } \hat{\boldsymbol{\theta}} \in \mathcal{S}_{\text{m}\delta} \setminus \mathring{\mathcal{S}}_{\text{m}} \text{ and } \nabla g_{\text{m}}^T\boldsymbol{\varrho} > 0. \end{cases} \tag{49}$$

Here, the matrix $\boldsymbol{K}_{\text{m}}$ is positive definite, $c(\hat{\boldsymbol{\theta}}) = \min\{1, \delta^{-1}g_{\text{m}}(\hat{\boldsymbol{\theta}})\}$, $\mathcal{S}_{\text{m}} = \{\hat{\boldsymbol{\theta}} \in \mathbb{R}^6 \mid g_{\text{m}}(\hat{\boldsymbol{\theta}}) \le 0\}$, $\mathcal{S}_{\text{m}\delta} = \{\hat{\boldsymbol{\theta}} \in \mathbb{R}^6 \mid g_{\text{m}}(\hat{\boldsymbol{\theta}}) \le \delta\}$, and

$$g_{\text{m}}(\hat{\boldsymbol{\theta}}) = \left(\frac{2\hat{\psi}_1 - \gamma_{\min,1} - \gamma_{\max,1}}{\gamma_{\max,1} - \gamma_{\min,1}}\right)^{2n} + \left(\frac{\hat{\psi}_2}{\gamma_2}\right)^{2n} + \left(\frac{\hat{\psi}_3}{\gamma_3}\right)^{2n} + \left(\frac{2\hat{\psi}_4 - \gamma_{\min,4} - \gamma_{\max,4}}{\gamma_{\max,4} - \gamma_{\min,4}}\right)^{2n} + \left(\frac{\hat{\psi}_5}{\gamma_5}\right)^{2n} + \left(\frac{\hat{\psi}_6}{\gamma_6}\right)^{2n} - 1, \tag{50}$$

where n can be any positive integer and δ is a real positive parameter.

In the following proposition, we summarize the properties of the RLS-based adaptation law with parameter projection.

Proposition 2. *Assume matrices $\boldsymbol{Q}_1 \succ \boldsymbol{0}$, $\boldsymbol{Q}_3 \succ \boldsymbol{0}$, and $\boldsymbol{H}(t) \succ \boldsymbol{0}$, for all $t \ge t_0$; a control input with the form in (34); and, the adaptation laws in (47) and (48). Then, the system specified by (30) and (31) is guaranteed to satisfy that*

- $\tilde{\boldsymbol{\theta}} \in \mathcal{L}_\infty$.
- $\boldsymbol{\varepsilon}$ and $\dot{\hat{\boldsymbol{\theta}}} \in \mathcal{L}_\infty \cap \mathcal{L}_2$.
- $\boldsymbol{e}_{\boldsymbol{\omega}}$, $\boldsymbol{v}$, and $\boldsymbol{z} \in \mathcal{L}_\infty$.

Proof. See Appendix A.2. □

Last in this section, we state additional mathematical properties of the closed-loop system in the form of another proposition.

Proposition 3. *All the signals associated with the closed-loop adaptive system consisting of the open-loop plant specified by (30) and (31), the controller in (34), the filters in (43) and (44), and the adaptation laws in (47) and (48) are globally uniformly bounded provided that the parameters $\boldsymbol{K}_1$, $\boldsymbol{K}_2$, $\boldsymbol{K}_4$, $\boldsymbol{Q}_1$, $\boldsymbol{Q}_3$, and λ, and the reference signal $\boldsymbol{\omega}_{\text{d}}(t)$ are chosen such that the conditions $\boldsymbol{Q}_1 \succ \boldsymbol{0}$, $\boldsymbol{Q}_3 \succ \boldsymbol{0}$, and $\boldsymbol{H}(t) \succ \boldsymbol{0}$, for all $t \ge t_0$, are satisfied. Moreover, $\lim_{t\to\infty}\boldsymbol{z}(t) = \boldsymbol{0}$, $\lim_{t\to\infty}\boldsymbol{v}(t) = \boldsymbol{0}$, and global asymptotic tracking is achieved. Namely,*

$$\lim_{t\to\infty}\boldsymbol{e}_{\boldsymbol{\omega}}(t) = \lim_{t\to\infty}[\boldsymbol{\omega}(t) - \boldsymbol{\omega}_{\text{d}}(t)] = \boldsymbol{0}. \tag{51}$$

Proof. See Appendix A.3. □

4.3. Attitude analysis

In this section, we show that the attitude error remains bounded during the execution of an aerobatic maneuver controlled with either of the two proposed adaptive schemes. As stated in Section 3.2, Θ_{e} denotes the rotation angle about the corresponding Euler axis to reach $\mathcal{I}$ from $\mathcal{B}$. Here, the Euler axis of rotation is specified using the coordinate unit vector $\boldsymbol{a}_{\text{e}}$, which has its components expressed in both $\mathcal{B}$ and $\mathcal{I}$. Thus, from basic quaternion algebra, we know that $e_0 = \cos\frac{\Theta_{\text{e}}}{2}$ and $\boldsymbol{e}_1 = -\sin\frac{\Theta_{\text{e}}}{2}\cdot\boldsymbol{a}_{\text{e}}$, which, using (10), allows us to conclude that

$$\dot{e}_0 = -\frac{\dot{\Theta}_{\text{e}}}{2}\sin\frac{\Theta_{\text{e}}}{2} = \frac{1}{2}\sin\frac{\Theta_{\text{e}}}{2}\cdot\boldsymbol{a}_{\text{e}}^T[\boldsymbol{\omega} - \bar{\boldsymbol{\omega}}_{\text{d}}]. \tag{52}$$

Hence, under the assumption that $\Theta_{\text{e}} \neq 0$, we obtain the relationship

$$\dot{\Theta}_{\text{e}} = -\boldsymbol{a}_{\text{e}}^T[\boldsymbol{\omega} - \bar{\boldsymbol{\omega}}_{\text{d}}] = -\boldsymbol{a}_{\text{e}}^T\boldsymbol{e}_{\boldsymbol{\omega}}, \tag{53}$$

in which we use the property that the vectors $\boldsymbol{\omega}_{\text{d}}$ and $\bar{\boldsymbol{\omega}}_{\text{d}}$ have the same components. Next, recalling that $|\boldsymbol{a}_{\text{e}}|_2 = 1$, directly from (53), it follows that

$$\dot{\Theta}_{\text{e}} \le \left|\dot{\Theta}_{\text{e}}\right| \le |\boldsymbol{e}_{\boldsymbol{\omega}}|_2. \tag{54}$$

Furthermore, integrating both sides of (54), we obtain that

$$\Theta_{\text{e}}(t) \le \Theta_{\text{e}}(t_0) + \int_{t_0}^{t}|\boldsymbol{e}_{\boldsymbol{\omega}}(\sigma)|_2\,d\sigma, \tag{55}$$

where $t_0 \le t \le t_{\text{f}}$, and t_0 and t_{f} denote the start and end times of the aerobatic maneuver, respectively. Here, $\Theta_{\text{e}}(t_0)$ is the attitude-angle error at the start of the maneuver, which can be regulated to zero during the climb phase described in Section 2.3 using a simple LTI controller because in this condition the attitude of the UAV remains near the hovering state.

Note that for a finite $\Theta_{\text{e}}(t_0)$, it follows directly from (55) that the attitude error, $\Theta_{\text{e}}(t)$, remains bounded during an aerobatic maneuver because $\boldsymbol{e}_{\boldsymbol{\omega}}(t)$ was proven to remain bounded and converge to zero asymptotically as $t \to \infty$. In other words, the dynamics of the attitude error does not have a finite escape time. This conclusion is extremely relevant because, considering that the total duration of a maneuver in the class studied in this paper is normally less than one second, it is important to ensure that $\Theta_{\text{e}}(t_{\text{f}})$ is bounded and sufficiently small such that the vehicle can restabilize its attitude and stop its rapid descent during the DR phase. This analytical finding is consistent with experimental observations (see Section 5), according to which both proposed adaptive control schemes produce very small final attitude errors $\Theta_{\text{e}}(t_{\text{f}})$ because the angular-velocity oscillations and overshoot caused by undesired aerodynamic effects are effectively counteracted by the controllers. Consistent with this notion, we quantify controller performance during aerobatic flight using the *performance figure of merit* (PFM)

$$\Lambda = \int_{t_0}^{t_{\text{f}}}|\boldsymbol{e}_{\boldsymbol{\omega}}(\sigma)|_2\,d\sigma, \tag{56}$$

which is also an upper bound for the attitude control error. Clearly, a smaller Λ represents a better performance.

4.4. Summary statements on the proposed control schemes

In Sections 4.1 and 4.2, we proposed two different adaptive control schemes capable of compensating for undesired aerodynamic effects. The first method is Lyapunov-based. In this case, the controller, specified by (18), and adaptation laws, given by (24) and (25), were derived from a single *proto*-Lyapunov function. The second method is modular. In this case, the control input, given by (34), was designed such that the ISS property is guaranteed, and the adaptation laws, given by (47) and (48), were derived separately from the controller, using the static linear parametric model specified by (45). Consistent with this modular approach, there exist other potential adaptation laws for the same parametric model.

5. Experimental results

5.1. Experimental platform

The quadrotor UAV used in the experiments presented here is the Crazyflie 2.0[6] shown in Fig. 1, which weighs 28 g including the battery, has a propeller-tip-to-propeller-tip distance of 14 cm, and exhibits a maximum thrust-to-weight ratio of 1.9. During the execution of an aerobatic maneuver, this quadrotor operates completely autonomously. Further details about the UAV platform and experimental setup can be found in Chen and Pérez-Arancibia (2016, 2017).

5.2. Maneuvers implemented experimentally

We implemented both the Lyapunov-based and modular adaptive controllers on the quadrotor platform to perform three different types of aerobatic flights: a triple-flip maneuver, a Pugachev's cobra, and a mixed-flip maneuver. Additionally, the linear controller specified by (13), which disregards the LTV actuator dynamics of the system, was implemented experimentally for the purpose of comparison. The triple-flip maneuver is defined as a 1080° rotation about the $\boldsymbol{b}_1$ axis with a maximum angular speed of $1800^\circ \cdot \mathrm{s}^{-1}$; the Pugachev's cobra is defined as a 180° rotation about the $\boldsymbol{b}_1$ axis, followed by a 180° rotation in the opposite direction with a maximum angular speed of $1000^\circ \cdot \mathrm{s}^{-1}$; and, the mixed-flip maneuver is defined as a sequence of rotations according to which the UAV rotates 140° about the $\boldsymbol{b}_1$ axis first, then 180° about the $\boldsymbol{b}_2$ axis, and finally 40° about the $-\boldsymbol{b}_1$ axis in order to return to a hovering state, while operating at a maximum angular speed of $1000^\circ \cdot \mathrm{s}^{-1}$. Each of these three maneuvers is performed in less than one second and, as a consequence, the high angular speed required for its execution induces the generation of significant and complex local airflow fields around the propellers of the controlled UAV platform.

5.3. Torque estimation and implementation of the adaptive schemes

Directly from (3), the torques acting on the UAV are estimated using the relationship $\boldsymbol{\tau} = \boldsymbol{J}\dot{\boldsymbol{\omega}} + \boldsymbol{\omega} \times \boldsymbol{J}\boldsymbol{\omega}$, where the angular acceleration, $\dot{\boldsymbol{\omega}}$, is calculated using the nonlinear derivative method in Levant (2003), which is based on the utilization of the measured angular velocity $\boldsymbol{\omega}$. The quadrotor UAV used in the experiments has a miniaturized size and, therefore, limited onboard computational resources. For this reason, to reduce the real-time computational cost and increase the sample-and-hold frequency of execution of the control loops, the projection algorithms used to implement both adaptive methods were simplified to become component-wise saturations, as already discussed in Chen and Pérez-Arancibia (2018). Additionally, to avoid saturation of the propeller motors, the algorithms that compute the control signals in both adaptive methods, respectively specified by (18) and (34), were implemented only on the axis that tracks the nonzero-reference signals and the linear controller given by (13) was implemented on the other two axes that track the zero-reference signals. This approach is reasonable because the axes that track zero-reference signals encounter negligible undesired effects induced by time-varying aerodynamic coefficients and torque latency.

[6] https://store.bitcraze.io/products/crazyflie-2-0.

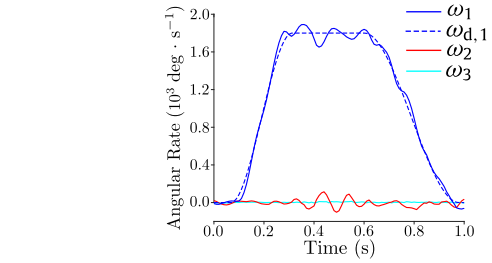

(a) Linear control.

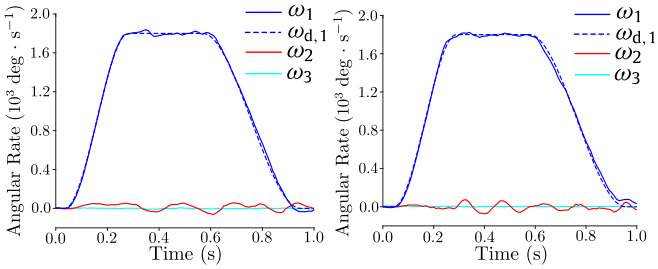

(b) Lyapunov-based adaptive control. (c) Modular adaptive control.

Fig. 2. Triple flips executed using three different controllers. (a) Experimental data obtained using the linear controller specified by (13). The corresponding PFM is $\Lambda = 0.9391$ rad. (b) Experimental data obtained using the Lyapunov-based adaptive controller specified by (18). The corresponding PFM is $\Lambda = 0.6397$ rad. (c) Experimental data obtained using the modular adaptive controller specified by (34). The corresponding PFM is $\Lambda = 0.6286$ rad. Since, in these three cases, $\omega_{\mathrm{d},2}(t) = \omega_{\mathrm{d},3}(t) = 0$, for all t, these signals are not plotted.

5.4. Experimental results

During the flight experiments, the three aerobatic maneuvers described in Section 5.2 were performed employing the Lyapunov-based and modular-based adaptive control schemes presented in Section 4, and also the linear controller specified by (13), which was implemented for comparison purposes. The experimental results corresponding to the three different maneuvers, obtained with the three different controllers, are shown in Figs. 2, 3, and 4, respectively. In all three maneuver cases, it is clear that the aerobatic performance obtained with the linear controller reflects the inability of this method to counteract noticeable angular-velocity oscillations and significant overshoot, which we believe are caused by unmodeled time-varying actuator dynamics resulting from aerodynamic-coefficient and torque-latency variations. This linear controller was designed using the nominal dynamics of the system only, according to the method in Chen and Pérez-Arancibia (2020), without considering the LTV model of the actuator presented in Section 3.

In contrast with the results obtained using the LTI controller, in all three maneuver cases, the aerobatic performance achieved with both adaptive controllers reflect their ability to significantly counteract undesired angular-velocity oscillations and overshoot.

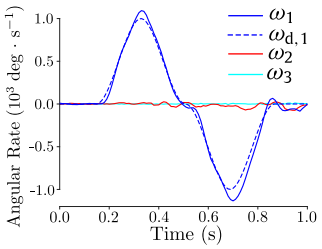

(a) Linear control.

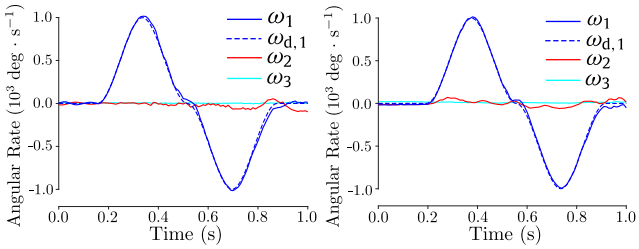

(b) Lyapunov-based adaptive control. (c) Modular adaptive control.

Fig. 3. Experimental Pugachev's cobras executed using three different controllers. (a) Data obtained using the linear controller specified by (13). The corresponding PFM is $\Lambda = 0.7413$ rad. (b) Data obtained using the Lyapunov-based adaptive controller specified by (18). The corresponding PFM is $\Lambda = 0.4625$ rad. (c) Data obtained using the modular adaptive controller specified by (34). The corresponding PFM is $\Lambda = 0.4888$ rad. Since, in these three cases, $\omega_{d,2}(t) = \omega_{d,3}(t) = 0$, for all t, these signals are not plotted.

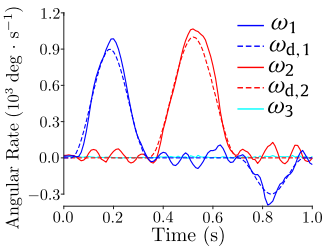

(a) Linear control.

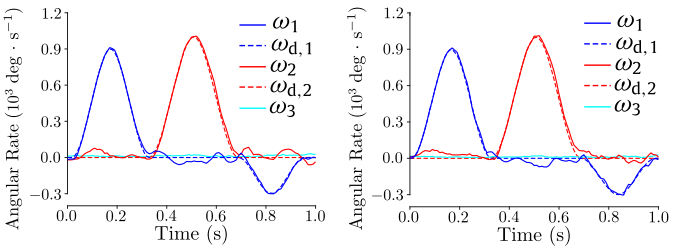

(b) Lyapunov-based adaptive control. (c) Modular adaptive control.

Fig. 4. Experimental mixed flips executed using three different controllers. (a) Data obtained using the linear controller specified by (13). The corresponding PFM is $\Lambda = 1.1497$ rad. (b) Data obtained using the Lyapunov-based adaptive controller specified by (18). The corresponding PFM is $\Lambda = 0.6826$ rad. (c) Data obtained using the modular adaptive controller specified by (34). The corresponding PFM is $\Lambda = 0.6920$ rad. Since, in these three cases, $\omega_{d,3}(t) = 0$, for all t, this signal is not plotted.

Quantitatively, the Lyapunov-based adaptive scheme reduced the PFM values, Λ, corresponding to the maneuvers in Figs. 2, 3, and 4, with respect to those obtained with the linear controller by 31.88 %, 37.61 %, and 40.63 %, respectively. Similarly, the modular adaptive scheme reduced the PFM values corresponding to the three studied maneuvers by 33.06 %, 34.06 %, and 39.81 %, respectively. These results also provide indirect evidence about the correctness and accuracy of the LTV model introduced to describe undesired aerodynamic effects affecting the actuator dynamics of the controlled UAV. Video footage that shows experimental results obtained using both proposed adaptive control schemes during the execution of the three different aerobatic maneuvers discussed above can be seen in the supplementary movie accompanying this paper.

Clearly, the aerobatic-performance results obtained with both adaptive control schemes are similar to each other. However, there exist many differences from the implementation perspective. In particular, the Lyapunov-based controller is significantly more efficient than the modular controller from the numerical perspective because it requires the definition of a fewer number of variables and the computational complexity is significantly lower. On the other hand, the modular scheme is flexible enough to be implemented with different adaptation laws for different experimental situations while the adaptation law of the Lyapunov-based method is fixed. Last, to test and demonstrate the performance robustness of the proposed adaptive schemes, we selected two flight experiments during which the tested UAV was controlled to perform several consecutive aerobatic maneuvers. Specifically, Fig. 5(a) shows that the tested quadrotor UAV is able to continually perform eleven consecutive Pugachev's cobra maneuvers without crashing or stalling until its battery is entirely discharged, when controlled using the Lyapunov-based scheme. Similarly, Fig. 5(b) shows that the tested quadrotor UAV is able to continually perform twelve consecutive mixed-flip maneuvers without crashing or stalling until its battery is entirely discharged, when controlled using the modular scheme.

6. Conclusions

We presented two different adaptive control schemes to enable a VTOL UAV to perform aerobatic maneuvers defined by extremely high angular and translational velocities, which generate complex interactions of the vehicle with the surrounding flow fields. First, we introduced an LTV model to describe the actuator dynamics of the system, which explicitly accounts for undesirable effects produced by aerodynamic-coefficient and torque-latency time-variations caused by the high speeds associated with rapid aerobatic maneuvers. Then, we presented a Lyapunov-based adaptive control scheme, which was developed to explicitly compensate for the negative effects generated by time-varying actuator dynamics. Next, to add flexibility regarding the adaptation law of the control scheme, we introduced a modular adaptive approach, which was experimentally demonstrated to achieve a flight performance similar to that obtained with the Lyapunov-based method. Furthermore, both proposed adaptive control methods were theoretically proven to stabilize the closed-loop system globally. Last, we presented data, obtained through three representative aerobatic-flight experiments, that compellingly demonstrate the effectiveness and robustness of the two proposed adaptive control methods. These experimental data also indirectly provide evidence about the correctness and accuracy of the LTV model introduced to describe the actuator dynamics of the system.

Appendix. Proofs of the propositions

A.1. Proof of Proposition 1

From (37), it immediately follows that

$$\dot{V}_2 \leq -(1-c_h)\,\lambda_h\,|\boldsymbol{x}|_2 - \left(c_h\lambda_h\,|\boldsymbol{x}|_2 - \frac{1}{4}\left(\tilde{a}^2+\tilde{b}^2\right)\right), \qquad (A.1)$$

where $\lambda_h = \min_{t\geq t_0}\{\lambda_{\min}\{\boldsymbol{H}(t)\}\} > 0$; and $0 < c_h < 1$. It is straightforward to see that $\dot{V}_2 \leq 0$ whenever $|\boldsymbol{x}|_2 \geq \frac{1}{4c_h\lambda_h}\left(\tilde{a}^2+\tilde{b}^2\right)$. Hence,

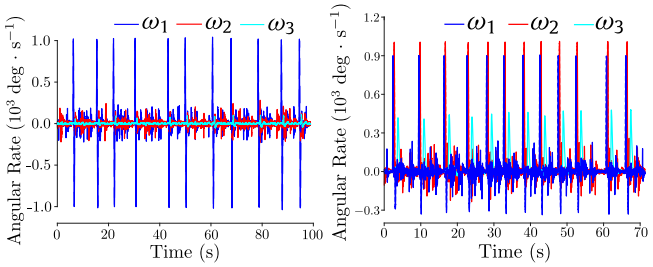

(a) Lyapunov-based adaptive control. (b) Modular adaptive control.

Fig. 5. Consecutive aerobatic maneuvers. (a) Data corresponding to eleven consecutive Pugachev's cobras executed using the Lyapunov-based adaptive controller specified by (18). (b) Data corresponding to twelve consecutive mixed flips executed using the modular adaptive controller specified by (34).

from Theorem C.2 in Krstić et al. (1995) and the Claim on Page 441 of Sontag (1989), the proposition follows immediately.

A.2. Proof of Proposition 2

In this case, we first define the candidate Lyapunov function $V_3 = \tilde{\boldsymbol{\theta}}^T \boldsymbol{P}^{-1}\tilde{\boldsymbol{\theta}} + \frac{1}{2c_0}\tilde{\boldsymbol{\varepsilon}}^T\tilde{\boldsymbol{\varepsilon}}$, where $c_0 = \lambda_{\min}\{\boldsymbol{K}_3\}$, and consider the instance when $\dot{\boldsymbol{P}} \neq 0$. To continue, we take the time derivative of V_3 and use the property that $-\tilde{\boldsymbol{\theta}}^T\boldsymbol{P}^{-1}\text{Proj}(\boldsymbol{\varrho}) \leq -\tilde{\boldsymbol{\theta}}^T\boldsymbol{P}^{-1}\boldsymbol{\varrho}$ (Krstić et al., 1995, Lemma E.1) to obtain that

$$\dot{V}_3 \leq \frac{\tilde{\boldsymbol{\theta}}^T\boldsymbol{\Gamma}\left[-2\boldsymbol{\varepsilon} + \boldsymbol{\Gamma}^T\tilde{\boldsymbol{\theta}}\right]}{1+\nu\,\text{tr}\{\boldsymbol{\Gamma}^T\boldsymbol{P}\boldsymbol{\Gamma}\}} - \beta\tilde{\boldsymbol{\theta}}^T\boldsymbol{P}^{-1}\tilde{\boldsymbol{\theta}} - \tilde{\boldsymbol{\varepsilon}}^T\tilde{\boldsymbol{\varepsilon}}. \tag{A.2}$$

Then, by substituting $\boldsymbol{\Gamma}^T\tilde{\boldsymbol{\theta}} = \boldsymbol{\varepsilon} - \tilde{\boldsymbol{\varepsilon}}$ into (A.2), we get that

$$\dot{V}_3 \leq -\frac{\boldsymbol{\varepsilon}^T\boldsymbol{\varepsilon}}{1+\nu\,\text{tr}\{\boldsymbol{\Gamma}^T\boldsymbol{P}\boldsymbol{\Gamma}\}} - \beta\tilde{\boldsymbol{\theta}}^T\boldsymbol{P}^{-1}\tilde{\boldsymbol{\theta}}. \tag{A.3}$$

On the other hand, when $\dot{\boldsymbol{P}} = \boldsymbol{0}$, we have that

$$\begin{aligned}\dot{V}_3 &\leq \frac{-2[\boldsymbol{\varepsilon}-\tilde{\boldsymbol{\varepsilon}}]^T\boldsymbol{\varepsilon}}{1+\nu\,\text{tr}\{\boldsymbol{\Gamma}^T\boldsymbol{P}\boldsymbol{\Gamma}\}} - \tilde{\boldsymbol{\varepsilon}}^T\tilde{\boldsymbol{\varepsilon}} \\ &\leq \frac{-\boldsymbol{\varepsilon}^T\boldsymbol{\varepsilon}}{1+\nu\,\text{tr}\{\boldsymbol{\Gamma}^T\boldsymbol{P}\boldsymbol{\Gamma}\}} - \left|\frac{\boldsymbol{\varepsilon}}{\sqrt{1+\nu\,\text{tr}\{\boldsymbol{\Gamma}^T\boldsymbol{P}\boldsymbol{\Gamma}\}}} - \tilde{\boldsymbol{\varepsilon}}\right|_2^2 \\ &\leq \frac{-\boldsymbol{\varepsilon}^T\boldsymbol{\varepsilon}}{1+\nu\,\text{tr}\{\boldsymbol{\Gamma}^T\boldsymbol{P}\boldsymbol{\Gamma}\}}.\end{aligned} \tag{A.4}$$

Therefore, considering that $\boldsymbol{P}^{-1}$ is positive definite, it follows that $\tilde{\boldsymbol{\theta}} \in \mathcal{L}_\infty$ and $\left(1+\nu\,\text{tr}\{\boldsymbol{\Gamma}^T\boldsymbol{P}\boldsymbol{\Gamma}\}\right)^{-\frac{1}{2}}\boldsymbol{\varepsilon} \in \mathcal{L}_2$. Then, the boundedness of $\tilde{\boldsymbol{\theta}}$ implies that $\tilde{a}$ and $\tilde{b} \in \mathcal{L}_\infty$. Also, directly from Proposition 1, it follows that $\boldsymbol{e}_{\boldsymbol{\omega}}$, $\boldsymbol{v}$, and $\boldsymbol{z} \in \mathcal{L}_\infty$; and, consequently, that $\boldsymbol{W}$ and $\boldsymbol{\Gamma} \in \mathcal{L}_\infty$. Furthermore, using the inequality

$$\int_{t_0}^{\infty}|\boldsymbol{\varepsilon}|_2^2\,dt \leq \left|1+\nu\,\text{tr}\{\boldsymbol{\Gamma}^T\boldsymbol{P}\boldsymbol{\Gamma}\}\right|_\infty \int_{t_0}^{\infty}\frac{|\boldsymbol{\varepsilon}|_2^2}{1+\nu\,\text{tr}\{\boldsymbol{\Gamma}^T\boldsymbol{P}\boldsymbol{\Gamma}\}} < \infty, \tag{A.5}$$

it can be shown that $\boldsymbol{\varepsilon} \in \mathcal{L}_2$. Similarly, we can prove that $\dot{\tilde{\boldsymbol{\theta}}} \in \mathcal{L}_2$ by recalling that the projection algorithm in (47) satisfies that $\text{Proj}(\boldsymbol{\varrho})^T\boldsymbol{K}_{\text{m}}^{-1}\text{Proj}(\boldsymbol{\varrho}) \leq \boldsymbol{\varrho}^T\boldsymbol{K}_{\text{m}}^{-1}\boldsymbol{\varrho}$, for all $\hat{\boldsymbol{\theta}} \in \mathcal{S}_{\text{m}\delta}$ (Krstić et al., 1995), $\boldsymbol{\varepsilon} \in \mathcal{L}_2$, and $\frac{\boldsymbol{P}\boldsymbol{\Gamma}}{1+\nu\,\text{tr}\{\boldsymbol{\Gamma}^T\boldsymbol{P}\boldsymbol{\Gamma}\}}$ is bounded. Last, considering the previous developments in this appendix, (47), and that $\boldsymbol{\varepsilon} = \boldsymbol{\Gamma}^T\tilde{\boldsymbol{\theta}} + \tilde{\boldsymbol{\varepsilon}}$, we conclude that $\boldsymbol{\varepsilon}$ and $\dot{\tilde{\boldsymbol{\theta}}} \in \mathcal{L}_\infty$.

A.3. Proof of Proposition 3

From expressions (37) and (A.1), it immediately follows that $|\boldsymbol{x}|_2 \leq \max\left\{|\boldsymbol{x}(t_0)|_2\,,\,\frac{1}{4c_{\text{h}}\lambda_{\text{h}}}\left(\tilde{a}^2+\tilde{b}^2\right)\right\}$. Also, it can be shown that $\tilde{a}^2+\tilde{b}^2 \leq \left(1+\sigma_1^2+\sigma_2^2\right)\max\left\{\left|\tilde{\boldsymbol{\theta}}_1\right|_2^2 + \left|\tilde{\boldsymbol{\theta}}_2\right|_2^2\right\}$, in which the term $\max\left\{\left|\tilde{\boldsymbol{\theta}}_1\right|_2^2 + \left|\tilde{\boldsymbol{\theta}}_2\right|_2^2\right\}$ is bounded because $\hat{\boldsymbol{\theta}}$ is bounded. Next, by using Lemma F.4 in Krstić et al. (1995), we conclude that $\boldsymbol{z} - \boldsymbol{\Gamma}^T\tilde{\boldsymbol{\theta}} \in \mathcal{L}_2$. Also, it follows that $\boldsymbol{\Gamma}^T\tilde{\boldsymbol{\theta}} \in \mathcal{L}_2$ because $\boldsymbol{\Gamma}^T\tilde{\boldsymbol{\theta}} = \boldsymbol{\varepsilon} - \tilde{\boldsymbol{\varepsilon}}$, in which both $\boldsymbol{\varepsilon}$ and $\tilde{\boldsymbol{\varepsilon}} \in \mathcal{L}_2$. Therefore, $\boldsymbol{z} \in \mathcal{L}_2$. Additionally, $\dot{\boldsymbol{z}} \in \mathcal{L}_\infty$ because the terms on the right side of (39) satisfy that $\boldsymbol{W}^T\tilde{\boldsymbol{\theta}}$ and $\boldsymbol{A}_{\boldsymbol{z}}\boldsymbol{z} \in \mathcal{L}_\infty$. Thus, from Barbalat's lemma, we conclude that $\boldsymbol{z} \to \boldsymbol{0}$ as $t \to \infty$. Furthermore, by simply using the *strictly passive* property of the input-to-output system from $\boldsymbol{z}$ to $\boldsymbol{e}_{\boldsymbol{\omega}}$ and $\boldsymbol{v}$, we can show that $\boldsymbol{e}_{\boldsymbol{\omega}}$ and $\boldsymbol{v} \in \mathcal{L}_2$. In this case, we prove this property using the Lyapunov function $V_4 = \frac{1}{2}\boldsymbol{e}_{\boldsymbol{\omega}}^T\boldsymbol{J}\boldsymbol{e}_{\boldsymbol{\omega}} + \frac{1}{2}\boldsymbol{v}^T\boldsymbol{Q}_1\boldsymbol{v}$. First, we take the time derivative of V_4 and obtain that

$$\begin{aligned}\dot{V}_4 &\leq -\lambda_{\text{g}}\left(|\boldsymbol{e}_{\boldsymbol{\omega}}|_2^2 + |\boldsymbol{v}|_2^2\right) + \boldsymbol{e}_{\boldsymbol{\omega}}^T\boldsymbol{z} \\ &\leq -\lambda_{\text{g}}|\boldsymbol{v}|_2^2 - (1-c_1)\lambda_{\text{g}}|\boldsymbol{e}_{\boldsymbol{\omega}}|_2^2 + \frac{1}{4c_1\lambda_{\text{g}}}|\boldsymbol{z}|_2^2,\end{aligned} \tag{A.6}$$

where $\lambda_{\text{g}} = \min_{t\geq t_0}\lambda_{\min}\{\boldsymbol{G}(t)\}$ and $0 < c_1 < 1$. Last, integrating both sides of (A.6), we get that

$$\begin{aligned}&\lambda_{\text{g}}\int_{t_0}^{\infty}|\boldsymbol{v}|_2^2\,d\sigma + (1-c_1)\lambda_{\text{g}}\int_{t_0}^{\infty}|\boldsymbol{e}_{\boldsymbol{\omega}}|_2^2\,d\sigma \\ &\leq V_4(t_0) - V_4(\infty) + \frac{1}{4c_1\lambda_{\text{g}}}\int_{t_0}^{\infty}|\boldsymbol{z}|_2^2\,d\sigma.\end{aligned} \tag{A.7}$$

Now, by noticing that $\boldsymbol{z} \in \mathcal{L}_2$ and $V_4(\infty)$ is bounded because $\boldsymbol{e}_{\boldsymbol{\omega}}$ and $\boldsymbol{v}$ are bounded, we conclude from (A.6) that $\boldsymbol{e}_{\boldsymbol{\omega}}$ and $\boldsymbol{v} \in \mathcal{L}_2$. Additionally, using (14) and (30), it can be shown that $\dot{\boldsymbol{e}}_{\boldsymbol{\omega}}$ and $\dot{\boldsymbol{v}} \in \mathcal{L}_\infty$. Thus, by directly applying Barbalat's lemma, we conclude that $\boldsymbol{e}_{\boldsymbol{\omega}}$ and $\boldsymbol{v} \to \boldsymbol{0}$ as $t \to \infty$.

Appendix B. Supplementary data

Supplementary material related to this article can be found online at https://doi.org/10.1016/j.automatica.2021.109922.

References

Abdessameud, A., & Tayebi, A. (2010). Global trajectory tracking control of VTOL-UAVs without linear velocity measurements. *Automatica*, *46*(6), 1053–1059.

Bangura, M., & Mahony, R. (2012). Nonlinear dynamic modeling for high performance control of a quadrotor. In *Proc. Australasian Conf. Robot. Automat. (ACRA)*. Wellington, New Zealand (pp. 1–10).

Bisheban, M., & Lee, T. (2021). Geometric adaptive control with neural networks for a quadrotor in wind fields. *IEEE Transactions on Control Systems Technology*, *29*(4), 1533–1548.

Boyd, S., & Vandenberghe, L. (2004). *Convex Optimization*. Cambridge, UK: Cambridge University Press.

Bristeau, P.-J., Martin, P., Salaün, E., & Petit, N. (2009). The role of propeller aerodynamics in the model of a quadrotor UAV. In *Proc. Eur. Control Conf. (ECC)*. Budapest, Hungary (pp. 683–688).

Cabecinhas, D., Cunha, R., & Silvestre, C. (2015). A globally stabilizing path following controller for rotorcraft with wind disturbance rejection. *IEEE Transactions on Control Systems Technology*, *23*(2), 708–714.

Chen, Y., & Pérez-Arancibia, N. O. (2016). Generation and real-time implementation of high-speed controlled maneuvers using an autonomous 19-gram quadrotor. In *Proc. IEEE Int. Conf. Robot. Automat. (ICRA)*. Stockholm, Sweden (pp. 3204–3211).

Chen, Y., & Pérez-Arancibia, N. O. (2017). Lyapunov-based controller synthesis and stability analysis for the execution of high-speed multi-flip quadrotor maneuvers. In *Proc. Amer. Control Conf. (ACC)*. Seattle, WA, USA (pp. 3599–3606).

Chen, Y., & Pérez-Arancibia, N. O. (2018). Nonlinear adaptive control of quadrotor multi-flipping maneuvers in the presence of time-varying torque latency. In *Proc. IEEE/RSJ Int. Conf. Intell. Robot. Syst. (IROS)*. Madrid, Spain (pp. 7845–7852).

Chen, Y., & Pérez-Arancibia, N. O. (2019). Adaptive control of aerobatic quadrotor maneuvers in the presence of propeller-aerodynamic-coefficient and torque-latency time-variations. In *Proc. IEEE Int. Conf. Robot. Automat. (ICRA)*. Montreal, QC, Canada (pp. 6447–6453).

Chen, Y., & Pérez-Arancibia, N. O. (2020). Controller synthesis and performance optimization for aerobatic quadrotor flight. *IEEE Transactions on Control Systems Technology*, *28*(6), 2204–2219.

Cheng, B., Tobalske, B. W., Powers, D. R., Hedrick, T. L., Wethington, S. M., Chiu, G. T. C., et al. (2016). Flight mechanics and control of escape manoeuvres in hummingbirds. I. Flight kinematics. *Journal of Experimental Biology*, *219*(22), 3518–3531.

Dudley, R. (2002). *The Biomechanics of Insect Flight: Form, Function, Evolution*. Princeton, NJ, USA: Princeton University Press.

Dydek, Z. T., Annaswamy, A. M., & Lavretsky, E. (2013). Adaptive control of quadrotor UAVs: A design trade study with flight evaluations. *IEEE Transactions on Control Systems Technology*, *21*(4), 1400–1406.

Fry, S. N., Sayaman, R., & Dickinson, M. H. (2003). The aerodynamics of free-flight maneuvers in *Drosophila*. *Science*, *300*(5618), 495–498.

Hua, M.-D., Hamel, T., Morin, P., & Samson, C. (2009). A control approach for thrust-propelled underactuated vehicles and its application to VTOL drones. *IEEE Transactions on Automatic Control*, *54*(8), 1837–1853.

Ioannou, P., & Fidan, B. (2006). *Adaptive Control Tutorial*. Philadelphia, PA, USA: SIAM.

Ioannou, P., & Sun, J. (2012). *Robust Adaptive Control*. Mineola, NY, USA: Dover.

Krstić, M., Kanellakopoulos, I., & Kokotović, P. (1995). *Nonlinear and Adaptive Control Design*. New York, NY, USA: Wiley.

Lee, D. (2012). Distributed backstepping control of multiple thrust-propelled vehicles on a balanced graph. *Automatica*, *48*(11), 2971–2977.

Lee, T., Leok, M., & McClamroch, N. H. (2010). Geometric tracking control of a quadrotor UAV on SE(3). In *Proc. 49th IEEE Conf. Decis. Control (CDC)*. Atlanta, GA, USA (pp. 5420–5425).

Leishman, G. J. (2006). *Principles of Helicopter Aerodynamics*. New York, NY, USA: Cambridge University Press.

Levant, A. (2003). Higher-order sliding modes, differentiation and output-feedback control. *International Journal of Control*, *76*(9–10), 924–941.

Lupashin, S., & D'Andrea, R. (2012). Adaptive fast open-loop maneuvers for quadrocopters. *Autonomous Robots*, *33*(1–2), 89–102.

Mahony, R., Kumar, V., & Corke, P. (2012). Multirotor aerial vehicles: Modeling, estimation, and control of quadrotor. *IEEE Robotics & Automation Magazine*, *19*(3), 20–32.

Mellinger, D., Michael, N., & Kumar, V. (2012). Trajectory generation and control for precise aggressive maneuvers with quadrotors. *International Journal of Robotics Research*, *31*(5), 664–674.

Roberts, A., & Tayebi, A. (2011). Adaptive position tracking of VTOL UAVs. *IEEE Transactions on Robotics*, *27*(1), 129–142.

Shyy, W., Lian, Y., Tang, J., Viieru, D., & Liu, H. (2007). *Aerodynamics of Low Reynolds Number flyers*. New York, NY, USA: Cambridge University Press.

Sontag, E. D. (1989). Smooth stabilization implies coprime factorization. *IEEE Transactions on Automatic Control*, *34*(4), 435–443.

Ying Chen received the B.S. degree in mechanical engineering from Beihang University, Beijing, China, in 2012, and the M.S. and Ph.D. degrees in mechanical engineering from the University of Southern California (USC), Los Angeles, CA, USA, in 2014 and 2019, respectively. From August 2014 to September 2019, he was a graduate researcher with the USC Autonomous Microrobotic Systems Laboratory (AMSL). Since October 2019, he has been with Intuitive Surgical Inc., Sunnyvale, CA, USA. His research interests include control theory, autonomous aerial robotic systems, microrobotics, and biologically-inspired engineering.

Néstor O. Pérez-Arancibia received the Ph.D. degree in mechanical engineering from the University of California, Los Angeles (UCLA), Los Angeles, CA, USA, in 2007. From October 2007 to March 2010, he was a Postdoctoral Scholar with the Laser Beam Control Laboratory and the Mechatronics and Controls Laboratory in the Mechanical and Aerospace Engineering Department at UCLA. From April 2010 to March 2013, he was a Postdoctoral Fellow, and from April 2013 to August 2013, he was a Research Associate with the Microrobotics Laboratory and the Wyss Institute for Biologically Inspired Engineering at Harvard University, Cambridge, MA, USA. From August 2013 to August 2021, he was a faculty member of the Department of Aerospace and Mechanical Engineering at the University of Southern California (USC), Los Angeles, CA, USA, where he founded and directed the Autonomous Microrobotic Systems Laboratory (AMSL). Since August 2021, Dr. Pérez-Arancibia has been a Flaherty Associate Professor in Engineering with the School of Mechanical and Materials Engineering at Washington State University (WSU), Pullman, WA, USA, where he continues to lead the AMSL. Currently, he is also an Associate Editor for Mechatronics, a journal of the International Federation of Automatic Control (IFAC). Many of Dr. Pérez-Arancibia's research papers have been nominated for, or won, best paper awards. Most recently, he won a 2020 IEEE Robotics and Automation Letters Best Paper Award. His current research and teaching interests include feedback control, mechatronics, microrobotics, soft robotics, and biologically-inspired engineering.